University College of London

Department of Physics and Astronomy

MSc Physics, MSc Thesis

COSMIC-RAY MUON TOMOGRAPHY FOR ANTI-TERRORISM APPLICATIONS

Author:

Linda Cremonesi

Supervisors:

Dr. Ryan Nichol

Dr. Ruben Saakyan

ACADEMIC YEAR 2010/2011

Abstract

This MSc Thesis explores the improvements which can be made when using the Multiple Coulomb Scattering of cosmic ray muons to create tomographic images of volumes, which may be otherwise undetectable. Feasible anti-terrorist applications may be obtained only with a high quality reconstruction algorithm and a short exposure time. This project has used and improved the algorithm of the CREAM TEA experiment of University College London (UCL), which relies on a Geant4 simulation of both target and detector and a Maximum Likelihood Expectation Maximization technique for the image reconstruction. Improvements in the latter algorithm can be achieved by measuring the muon energy and adding information about the displacement of the ray. Different ways of measuring the energies were analysed and two target sizes were inspected for the scattering and displacement algorithm. The result was a significant reduction of the noise, bringing a Figure of Merit five times larger than the one evaluated with standard methods, together with shortening the exposure time needed to detect a bomb (e.g. 5 seconds of exposure time for a 30 cm radius uranium target). These techniques can be adapted for smaller targets by simply reducing the size of the voxels.

Acknowledgements

This thesis would not have been successfully completed without the tremendous support of Dr Ryan Nichol, whose assistance was readily available throughout the year, from the start of this project.
Additionally, I am grateful to Asha Pooran, Patrick Begley and Chris Beach, for reading this report and providing feedback .
Furthermore, I would like to thank all my close friends for their interest in the project and the various points of view, hints and comments they willingly shared.
Finally, I am most appreciative of the continuous and constant support and encouragement provided by my parents, my brother and my sister throughout my academic and personal life.

Contents

Introduction

One of the most challenging problems in the area of international security is the control of large places of interchange, such as ports or train stations.
It is impossible to run high security systems similar to those present in an airport: for this reason, customs agencies currently employ radiation detectors and X-ray scanners at border crossings to preventing illicit transport of fissile material. However, X-ray radiography systems have various limitations, due to their potential harming effects on people (they cannot be used on occupied vehicles) and the low penetration of this radiation. This means that one could hide Special Nuclear Material by combining a small amount of lead or tungsten, with hydrogenous (polyethylene) and neutron absorbing (lithium or boron) shielding materials [1].
The cosmic ray muon tomography technique can provide a solution to this problem, by being able to discriminate between high-Z materials and hence to distinguish fissile material from the high-Z shielding.
The choice of using cosmic ray muons is principally due to the fact that they constitute a natural background radiation which is continuously bombarding Earth at a rate of 1 muon per cm^2 every minute [2] and it is *completely harmless radiation.*
In fact, cosmic ray radiation is principally composed of protons that interact in the upper atmosphere producing "showers" of particles, including pions. The charged pions then decay producing muons.
Muons passing through matter are slowed down and they can either be absorbed or deflected. The flux of absorbed muons is related to the density of the material, and measuring the difference in muon flux enables us to make a radiographic image of the volume. The first muon tomographies performed obtained very good results using only muon absorption information [3; 4; 5].
Despite the initial success of the absorption technique, the need for more precise results in a shorter exposure time led to a new approach to muon tomography: scattering information

began being used.
The trajectory of a charged particle (such as a muon) through any material is the result of the convolution of many small deflections due to Multiple Coulomb Scattering from the positively charged nuclei in the medium. The distribution of the net angular deflection is very sensitive to the charge of the atomic nuclei (Z): thus these deflections can be used to determine the density of the materials that the charged particles have traversed.
By using this new kind of cosmic ray muon tomography it is possible to reconstruct a 3D image of a volume to be analysed. Moreover, with regards to the anti-terrorism applications, it can be used to detect the presence of a high-Z object (such as a bomb), even when it is shielded by a water tank, a sheep cargo, a steel box or a high-Z material!

Part I

Background information

Chapter 1

Cosmic rays and muons passage through matter

Before going into the description of the muon tomography technique and the CREAM TEA experiment, an introduction on cosmic rays is needed.
The first part of this chapter presents the path of cosmic rays discovery through history, then their production, spectra and their interaction with the atmosphere which produces particle "showers".
The second part of the chapter presents a deeper description of the passage of particles through matter, introducing Multiple Coulomb Scattering, absorption information and the relation between the energy deposited by a particle and its momentum.

1.1 Cosmic rays: discovery, history and composition

1.1.1 Discovery and history

Cosmic rays are charged particles of unknown extraterrestrial origin which continuously bombard Earth.
The history of cosmic ray discovery began in 1900 when Elster and Geitel [6], and Wilson independently, found that pure air in a closed vessel possesses some electrical conductivity [7]. The year after, Wilson hypothesized that the residual ionization was due to some strongly penetrating radiation coming from the universe, but he soon rejected this as mere speculation [7].
Initially, the observed radiation was associated with gamma-ray emission from radioactive

elements. Later, in order to clarify the role of the radiation coming from Earth, the measuring devices were lifted to different altitudes - first up to the Eiffel tower [7] and then on balloon flights.
The 7^{th} of August 1912 is recognized as the date when of cosmic rays were truly discovered: on that day Hess made his most successful flight and suggested the following conclusion [7]: «*The results of present observations seem to be most readily explained by the assumption that a radiation of very high penetrating power enters our atmosphere from above and still produces in the lowest layers a part of the ionization observed in closed vessel.* »
Nonetheless, Hess' theory did not seem very convincing, because a German physicist Kolhöster [7], believed that the change in ionization rate with increasing height was due to temperature variations. These doubts vanished around 1925 when Kolhöster himself confirmed Hess' hypothesis, calling this radiation *Hohenstrahlung* (i.e. high altitude radiation) or *Hess'sche Strahlung* (i.e. Hess radiation), whereas Hess preferred the term *Ultra-gammastrahlung* (i.e. Ultra gamma radiation); the name "cosmic ray" was given in 1925 by Millikan [7], referring to fast charged particles of cosmic origin.
Later, sea-level observations of fast charged particles and the geomagnetic effect indicated that at least part of the cosmic ray flux consists of charged particles. Furthermore, Rossi demonstrated the ability of these charged particles to create secondary particles [7].

1.1.2 Charge and composition

In 1933, Rossi and Johnson, Alvarez and Compton established in their experiments the east-west asymmetry with a predominance of positive particles[1]. Even though, initially, these positively charged particles were believed to be positrons, between 1938 and 1940 it was clarified that the dominant particles in the composition of primary cosmic rays are protons. Basically, the electron-positron component of cosmic rays produces showers, whereas protons of the same energy do not: using devices with several lead-separated counters, it was found that primary particles produce almost no showers [7].
Studies in 1950-1952 recorded showers in a Wilson cloud chamber at high altitude and found that shower-producing particles (i.e. electrons, positrons and photons) were less than 1% of the total number of protons. Furthermore, during these years it was established that cosmic rays were principally composed of protons (about 90% of all primary cosmic rays),

[1]Positive and negative particles that hit the atmosphere are divided by the action of the magnetic field of the Earth. This means that if the number of positively and negatively charged particles is not the same, the particle fluxes from the east and from the west will not be identical and the so-called *east-west asymmetry* is observed.

Z	Element	F	Z	Element	F
1	H	540	13-14	Al-Si	0.19
2	He	26	15-16	P-S	0.03
3-5	Li-B	0.40	17-18	Cl-Ar	0.01
6-8	C-O	2.20	19-20	K-Ca	0.02
9-10	F-Ne	0.30	21-25	Sc-Mn	0.05

Table 1.1: Fractions of primary and secondary incident nuclei at 10.6 GeV/nucleon normalized to oxygen [8].

alpha particles (nearly 10% of the flux), nuclei of different elements (including iron) and positron-electrons (of the order of 1% of the total flux) [7].
Nowadays we know that about 79% of the primary nucleons are free protons, around 14% are alpha particles, and the rest are trace levels of different nuclei, as listed in Table 1.1. The fractions are nearly constant over the energy range from few GeV to 100 TeV [8].

1.1.3 Origin and primary spectra

Only around 40 years after Hess made his flights it was established that cosmic rays come from outer space to Earth, and they represent an ionizing "radiation" made up of protons and high-energy nuclei. Nonetheless, no cosmic ray sources are visible directly and, furthermore, cosmic rays near the Earth are isotropic! Even though almost a century has passed since Hess' discovery, the origin of cosmic rays still remain a mystery [9].
Nevertheless, the study of cosmic rays has always been of great importance to Physics. Until the early 1950s (in 1949, Fermi formulated a theory of the acceleration mechanism [10]) when the first high-energy accelerators were built, cosmic rays were the only source of particles with energy larger than a GeV, leading to the discovery of the positron (1932), muons (1937), pions (1947), kaons and hyperons (1953) [7]. Nonetheless, even today the study of cosmic rays is fundamental in both astrophysics and particle physics.
The cosmic radiation incident on the top of the atmosphere is composed of all the stable charged particles and nuclei with lifetimes of order 10^6 years or longer. Usually, we distinguish between:

- *Primary* cosmic rays: which represent all particles which are accelerated at astrophysical sources (such as protons, electrons, helium, carbon, oxygen, iron and other elements synthesized in stars);

- *Secondary* cosmic rays: which represent those particles produced when primaries interact with stellar gas (such as lithium, beryllium and boron, which are not abundant products of stellar nucleosynthesis; or larger fraction of antiprotons and positrons).

Figure 1.1(a) shows the flux of primary nuclei over the energy scale of 0.1 GeV to a thousand of TeV.
Actually, the cosmic radiation is "modulated" by the solar wind (the expanding magnetized plasma generated by the Sun) which decelerates and partially excludes the lower energy cosmic rays from the inner solar system. This causes the anti-correlation between the solar activity and the intensity of cosmic rays with energies below 10 GeV.
The intensity of incident primaries at the top of the atmosphere is given approximately by this formula [8]:

$$I_N(E) = 1.8 \times \left(\frac{E}{1\ \text{GeV}}\right)^{-\alpha} \frac{\text{nucleons}}{\text{m}^2\ \text{s sr GeV}} \tag{1.1}$$

where E is the energy per nucleon (in a range from several GeV to beyond 100 TeV) and $\alpha \equiv (\gamma + 1) = 2.7$ is the differential spectral index of the cosmic ray flux (γ is the integral spectral index). Figure 1.1(b) shows the fluxes of cosmic rays at different altitudes in the atmosphere.
Even though the fractions of primary nuclei are nearly constant in this energy range, the ratio of secondary to primary nuclei is observed to decrease with increasing energy: the lifetime of the cosmic rays in the galaxy decreases with energy [8].

1.2 Muons on Earth

The production of secondary muons by cosmic ray interactions is a central point in the muon tomography technique and thus in the CREAM TEA experiment. When cosmic ray protons pass through the atmosphere of the Earth they generate particle "showers" in which hadronic secondary particles (such as pions and kaons) are created. These are produced as nucleons interact with nitrogen and oxygen, and then they decay to muons as follows:

$$\pi^+/K^+ \rightarrow \mu^+ + \nu_\mu$$
$$\pi^-/K^- \rightarrow \mu^- + \overline{\nu_\mu}$$

Charged pions with high energies (above 100 GeV) can interact with nitrogen and oxygen producing additional cascades of secondary particles before decaying; whereas low energy

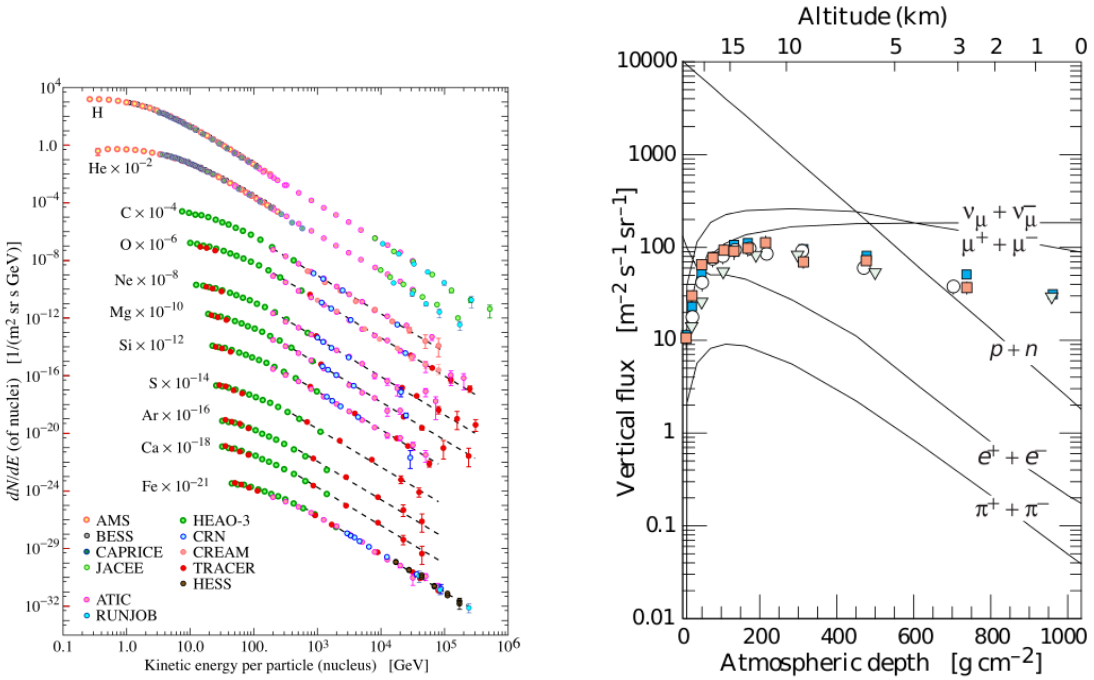

(a) (b)

Figure 1.1: (a) Major components of the primary cosmic radiation. (b) Lines represent the vertical fluxes of cosmic rays in the atmosphere with Energy $>$ 1 GeV, evaluated with Equation 1.1; the points show measurement of muons in the same energy range [8].

pions will more likely undergo weak decay before interacting with the atmosphere (e.g. a 1 GeV charged pion with a lifetime of 26 ns can travel only 55 meters) [11].
Most pions/kaons tend to decay in the upper atmosphere ($\sim$ 15 km) but muons with energy above 5 GeV can reach far below ground before decaying. This means that muons are the most readily measurable products of cosmic rays near the surface of the earth. The flux of muons striking the Earth at sea-level is 1 muon per cm^2 every minute [2].
The effects of the production spectrum, energy loss in the atmosphere and decay can be seen in the angular and energy distribution: the average energy of muons at the ground is $\approx$ 4 GeV.
Considering the energy spectrum, it is almost flat in the region before 1 GeV, between 10-100 GeV it steepens to reflect the primary spectrum and it steepens further at higher energies (since pions tend to interact in the atmosphere before they decay). For $E_\pi \gg 1$ TeV, the muon spectrum is one power steeper than the primary spectrum [8].
As regards the angular distribution, it is proportional to $\cos^2\theta$, which is typical of muons of $E_\mu \sim 3$ GeV. At large angles, low energy muons decay before reaching the ground and

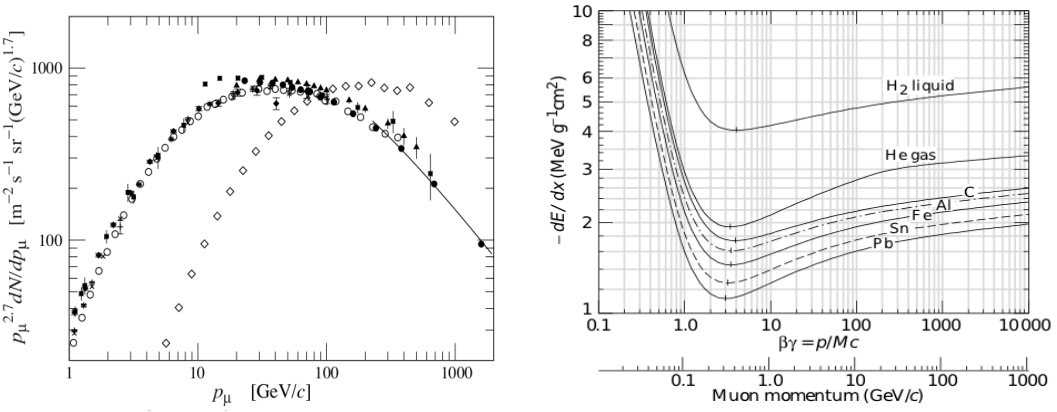

(a) (b)

Figure 1.2: (a) Spectrum of muons at $\theta = 0°$ for every point except $\diamond$ which represents $\theta = 75°$ [8]. (b) Average energy loss rate in liquid (bubble chamber) H, gaseous He, C, Al, Fe, Sn, and Pb [8].

high energy pions decay before interacting, hence the mean average energy increases. When muon decay is negligible ($E_\mu > 100/\cos\theta$ GeV) and the curvature of the Earth can be neglected ($\theta < 70°$), it holds this empirical formula [8]:

$$\frac{dN_\mu}{dE_\mu d\Omega} \approx \frac{0.14 E_\mu^{-2.7}}{\text{cm}^2 \text{ s sr GeV}} \left(\frac{1}{1 + \frac{1.1 E_\mu \cos\theta}{115 \text{ GeV}}} + \frac{0.054}{1 + \frac{1.1 E_\mu \cos\theta}{850 \text{ GeV}}} \right) \tag{1.2}$$

where the two different terms give the contribution of pions and kaons. The spectrum of muon momentum in different angles is shown in Figure 1.2(a).

1.3 Muons through matter

At sufficiently high energies, radiative processes become more important than ionization for all charged particles (for muons this "critical energy" occurs at several hundred GeV) and they dominate the energy loss. This can be written as a function of the amount of matter traversed:

$$-\frac{dE}{dx} = a(E) + b(E)E \tag{1.3}$$

where $a(E)$ is the ionization energy loss and $b(E)$ is the sum of bremsstrahlung, e^+e^- pair production and photo-nuclear contributions.

These functions vary slowly and we can consider them constant, so the mean range of

muons with initial energy E_0 is given by:

$$x_0 \approx \frac{1}{b} \ln \left(1 + \frac{E_0}{E_{\mu c}} \right) \tag{1.4}$$

where the muon "critical energy" $E_{\mu c}$ can be defined as the energy at which radiative and ionization losses are equal (i.e. $E_{\mu c} = a(E_{\mu c})/b(E_{\mu c})$): below $E_{\mu c}$ ionization losses dominate, above it radiative effects dominate.
We can now have a brief look at the energy loss probability distribution, because it will be useful when trying to find a way to estimate the muon momentum (in my project I will use the energy deposited in the scintillator planes to estimate the muon momentum). The energy loss probability distribution follows a Landau-Vavilov distribution and the most probable energy loss is described by this relation [8]:

$$\Delta_p = \xi \left[\ln \frac{2mc^2\beta^2\gamma^2}{I} + \ln \frac{\xi}{I} + j - \beta^2 - \delta(\beta\gamma) \right] \tag{1.5}$$

where $\xi = (K/2)\langle Z/A \rangle (x/\beta^2)$ MeV, x is the thickness in g cm^{-2}, $j = 0.2$ and the density effect correction $\delta(\beta\gamma)$ is given by:

$$\delta/2 \to \ln(\hbar\omega_p) + \ln \beta\gamma - 1/2 \tag{1.6}$$

in which $\hbar\omega_p$ is the plasma energy.

1.4 Multiple Coulomb Scattering

A muon passing through a material can sometimes be absorbed and other times be scattered. In this second case the particle traverses the material in a random path due to *Multiple Coulomb Scattering* and it emerges in a direction which forms with the initial direction the scattering angle θ, as shown in Figure 1.3(a).
The distribution of the deviation angle projected on a plane, is approximately a Gaussian distribution with zero mean value and root mean square σ as follows [12; 2]:

$$\sigma = \frac{13.6 \text{ MeV}}{\beta pc} \sqrt{\frac{x}{X_0}} \left[1 + 0.038 \ln \left(\frac{x}{X_0} \right) \right] \approx \frac{13.6 \text{ MeV/c}}{p} \sqrt{\frac{x}{X_0}} \tag{1.7}$$

where x is the thickness of the material, p is the muon momentum and X_0 is the radiation length which follows the formula [12]:

$$X_0 = \frac{716.4(\mathrm{g/cm^2})}{\rho} \frac{A}{Z(Z+1)\ln(287/\sqrt{Z})} \tag{1.8}$$

where ρ, A and Z are the density, atomic number and mass number of the material respectively.
The radiation length in a mixture or compound may be approximated by:

$$1/X_0 = \sum w_j/X_j \tag{1.9}$$

where w_j and X_j are the fractions by weight and the radiation length for the jth element. Equation 1.8 shows that the radiation length decreases with increasing Z; hence, for Equation 1.7 the standard deviation of the angular scattering distribution increases with Z. This Z sensitivity allows the muon tomography technique to distinguish high-Z (lead, tungsten, uranium) materials from medium-Z (iron, copper) and low-Z (water, concrete, plastic) materials simply by looking at the scattering angle distribution, as can be seen in Figure 1.3(b).

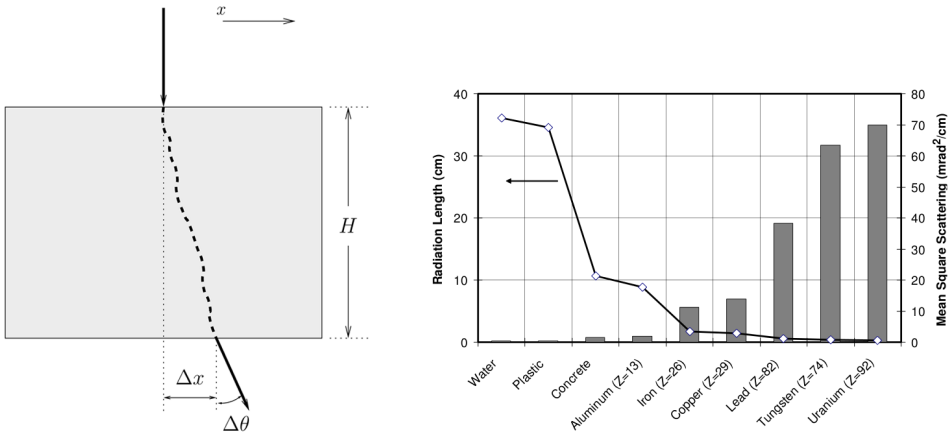

(a) (b)

Figure 1.3: (a) 2D projection of scattering and displacement used to describe multiple Coulomb scattering. (The magnitude of scattering is exaggerated) [13] (b) Radiation Length and Mean square scattering per unit depth of muons with energy 3 GeV. It is clear the Z-dependence of both these parameters [2].

Chapter 2

Muon tomography and CREAM TEA experiment

As presented in the Introduction of this Research Essay, the muon tomography technique can be used for the detection of hidden Special Nuclear Material in a short time, by using Multiple Coulomb Scattering of cosmic ray muons as a radiographic probe.
This Chapter presents the history of muon tomography research and its initial achievements; then I will explain the CREAM TEA experiment in depth, both in its detector design and the simulation program. Finally, I will describe the most important results achieved all around the World with this tomographic technique.

2.1 Muon tomography history and achievements

The idea of exploiting the natural background provided by cosmic ray muons for reconstructing a radiographic image was first introduced by E.P. George in 1955 [3]. He used the property that different materials absorb muons in different quantities in order to measure the depth of rock in an underground tunnel. Actually, he measured the attenuated cosmic ray flux inside the tunnel and the incident flux outside it, thus he inferred the rock depth from the ratio of these signals.
Following George's work, in 1970 the Nobel Prize Luis Alvarez [4] used the attenuation of the cosmic ray flux to look for hidden chambers inside the Chefren Pyramid in El Giza: unfortunately, he did not find any, but he managed to successfully use this technique.
More recent results see Nagamine in 1992 trying to predict volcanic eruption of Mt.Fugen and in 1995 mapping the inner structure of Mt. Tsukuba [5], both in Japan.

All these experiments used cosmic ray muon absorption to get a radiographic image of a region that would otherwise be inaccessible. Despite its initial success muon tomography was not studied in detail until a new way of approaching it was introduced.
This new form of cosmic ray muon tomography was based on Multiple Coulomb Scattering of particles as they pass through a material, as explained in Section 1.4. High energy muons travelling through material are not only absorbed, but can also be scattered. The deviation angle projected onto a plane has a Gaussian distribution around zero with a width that is related to the radiation length of the material. Looking at both scattering and absorption information it is possible to reconstruct a 3D image of objects. Moreover, the use of passive cosmic ray muons allows us to produce radiographic images of dense objects with *no artificial dose of radiation*.

2.2 Muon tomography principles

The general concept of muon tomography is illustrated in Figure 2.2. The experimental device is composed of a set of two or more planes placed above the volume to be analysed; these planes provide the position and angle of the incoming muon tracks in two orthogonal coordinates (this is necessary in order to have a 3D image of the volume).
Muon passing through the volume are scattered or absorbed by the material inside the volume, and then another set of detector planes provide the positions and angles of the outgoing muons.
With the information from the upper and lower detectors it is possible to reconstruct the muon path and get the scattering angle. Actually, the scattering angle distribution is stochastic, its mean is equal to zero and the root mean square is related to the scattering length of the penetrated material, as shown in Equation 1.7.
The principle behind this method is simple: regions of low density material will allow more muons to pass through without being scattered than regions of high density material. Hence, the 3D image is reconstructed by:

1. measuring the muon flux at different angles and positions over the target volume;
2. analysing differences in flux between particular angles and directions using standard techniques of tomography.

Furthermore, the probability of scattering decreases as the muon energy increases. Hence, for minimizing tracking errors we should consider muons with an energy large enough to

have a low probability of scattering through the material of interest.

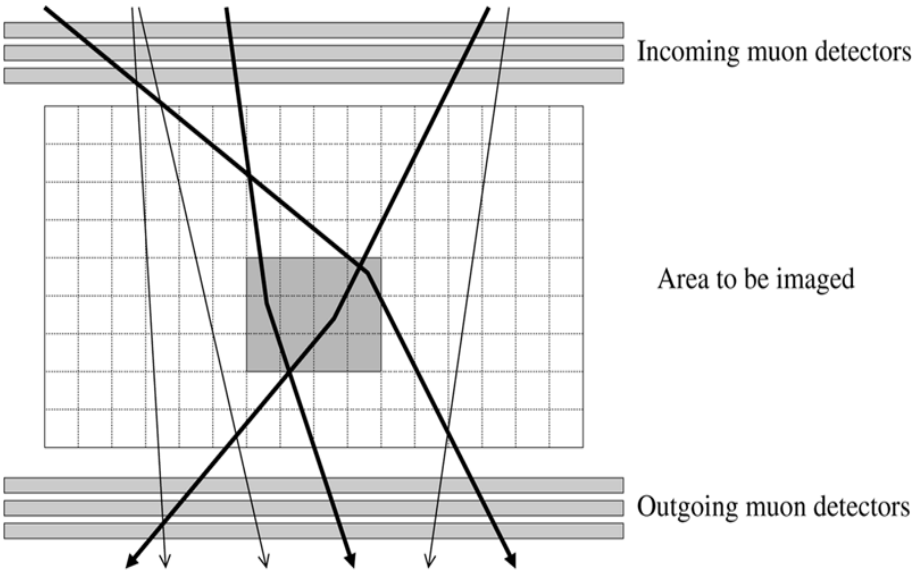

Figure 2.1: Muon tomography principle. Incoming and outgoing muon tracks (solid lines with arrows) are reconstructed by the set of muon detectors above and below the target volume. Muons passing through a high-Z object (black tracks) scatter more than muons going through air (grey tracks). Using the cosmic ray muon flux it is possible to reconstruct the geometry of the object and its density. (The magnitude of scattering is exaggerated) [13]

2.3 CREAM TEA experiment

The CREAM TEA experiment is part of the UCL High Energy Physics Department and the acronym means: **C**osmic **R**ays **E**xtensive **A**rea **M**apping for **T**errorism **E**vasion **A**pplications.

The aim of this experiment is to study and improve the muon tomography technique and find a way to detect hidden nuclear material, without using harmful radiation.

This research is done both using an experimental apparatus and a simulation program.

2.3.1 Detector design

The prototype used in the CREAM TEA experiment is similar to the general detector described in Section 2.2.

Scintillator planes made of polystyrene are used, hence there are no issues with safety, like

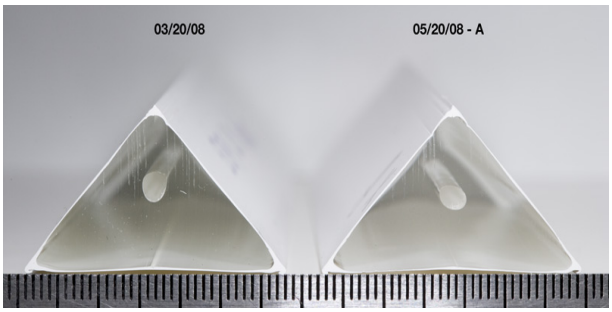

Figure 2.2: MINERVA style scintillator planes [15]

liquid or gas detectors.
There are two sets of scintillator planes that can be used with the prototype:

- 6 planes (3 with wires in x direction and 3 in y direction) of MINOS [14] style per side: 1 cm thick plastic scintillator segmented into 4.1 cm wide rectangles;
- 4 planes (2 with wires in x direction and 2 in y direction) of MINERVA [15] style per side: planes divided in 33 mm $\times$ 17 mm triangular strips to form a "toblerone" shape, as shown in Figure 2.2.

The latter has much improved position resolution as each muons hits multiple strips. Each plane has an area of 1 m^2; the distance between adjacent planes is 10 cm.
Odd planes have wires in the same direction and measure the muon trajectory in the x-z plane; whereas even planes have wires perpendicular to those of odd planes and measure trajectory on the y-z plane. In this way it is possible to produce a 3D image of the region within the apparatus.
The distance between the upper and lower planes is 1 meter, hence the probed volume is 1 m^3, making it suitable for the detection of small volumes of high-Z materials (steel, iron, copper, lead or uranium).
The electronic pulses produced by scintillator strips are readout by Photo Multipliers Tubes (PMTs) and acquired by digitalisation electronics. See Reference [11] for a deep description of the data acquisition system.

2.3.2 Simulation program

The simulation program uses Geant4[1] to simulate the detector configuration, along with interactions of muons with scintillator planes and the target inside the detector volume.
The detector simulated is bigger than the experimental apparatus described in Subsection 2.3.1: the scintillator planes have an area of 13×13 m^2, 650 strips per plane and 8 planes per side; the distance between above and below sets of planes is 13 m.
The characteristics of each plane are the same as the MINERVA scintillators, as described in Subsection 2.3.1.
Inside the detector volume it is possible to simulate different objects, for example:

- *container*: a 5 mm thick iron container with dimensions 2.44 m (x direction), 12.15 m (y direction) and 2.59 m (z direction);
- *water tank*: part of the volume of the container is filled with water;
- *steel box*: a steel box of user defined position, dimensions and thickness;
- *target*: a sphere of material, with density, position and dimensions defined by the user.

2.4 Data analysis, image reconstruction and quality

The current programme used by the CREAM TEA experiment is divided into 3 main stages:

1. *Simulation*
2. *Detector output*
3. *Image reconstruction*

2.4.1 Simulation

The simulation stage has been described in depth in Subsection 2.3.2: Geant4 simulates the detector, the target bomb and surrounding environment.

[1]Geant4 is a tool in the particle physics community for the simulation of the interaction of particles with matter. Applications of Geant4 are in high energy, nuclear and accelerator physics, as well as studies in medical and space science. [16]

In this stage, Geant4 simulates the interaction of muons with the top scintillator planes, the target/environment and the bottom scintillator planes. The outputs are in the form of ROOT [17] files with information of every particle (whether muons or particles created from muon interactions, such as electrons) passing through the scintillator planes.
The spectrum of generated muons has a momentum distribution falling as $p^{2.7}$ (very similar to the momentum distribution of cosmic ray muons) in a range of 0.1 to 1000 GeV/c.
Using Monte Carlo data is important, because it gives us "true" information about each event, that in a normal experiment we would not have. Even though we cannot use these pieces of information in reality, they are important to understand muon behaviour and interactions.

2.4.2 Detector output

In this stage the ROOT files produced by Geant4 are converted to the equivalent ROOT files that would be produced by a detector in reality: for each event the position hit on the scintillator plane, the energy deposited in each triangles and other important pieces of informations are registered.
This phase is important because it can approximate different scintillator types and strip sizes, and estimate their accuracy.

2.4.3 Image reconstruction

The output tree is then converted into histograms containing information about scattering (using the *Point of Closest Approach*) and absorption.

1. *Point of Closest Approach*: the PCA is an algorithm used to perform 2D and 3D radiography. Every muon takes a stochastic scattered path through a volume and its path is estimated looking at the energy deposited in the upper and lower planes: every triangle in which the muon deposited energy is a point where the muon passed. Since the scattering angle (estimated in two planes) is of order of milliradians, the path can be approximated by a straight line that connects the entry and exit points. Voxels (3D pixels) along this line are candidates for having scattered the ray passed through them.

   Now we make the assumption that the scattering was due to a single event and find its position by extrapolating the incident and scattered rays to their point of closest approach. The voxel found is filled with the signal value found by using the

information on the root mean square of the scattering angles and the momentum of the particles, using the Maximum Likelihood Expectation Maximization strategy [12] as described in Subsection 2.4.4, other voxels are filled with the correspondent value for air.
Each muon passing through the detector would contribute to form a 3D image of the volume inside it.
Figure 2.4.3 shows a 2D representation of the stages of the PCA algorithm; this is further explained in Reference [2].

2. *Absorption*: the absorption information is processed in a similar way. This time we take into consideration all the paths in the upper set of scintillator planes that do not arrive on the lower set of scintillator planes: those muons are likely to have been absorbed by the sample inside the volume. In order to understand in which voxel the muon has been absorbed it is possible to look at more paths together: if two lines cross in a voxel, it means that the muons are likely to have been absorbed at that point. That voxel is then filled with a signal value, this time proportional to the number of muons absorbed in that voxel.
For further information about the absorption technique see Reference [5].

The absorption and scattering trees are evaluated for long exposure time when the detector is empty, in order to produce high quality images of the background. When we have a target inside the volume, the muon exposure time has to be as short as possible (because the aim is to detect the presence of a material in a useful time).
Hence, it is possible to perform a background subtraction: the voxel content of the background histogram is subtracted from the value in each voxel of the target histogram, and if the difference is higher than a threshold, the output voxel is filled with that value. The background subtraction allows for a better image quality and to see the presence of high-Z materials more clearly even with short muon exposition time.

2.4.4 Maximum Likelihood Expectation Maximization strategy

For each muon, after reconstructing the path, the scattering angle is recorded as the i-th element s_i of the vector $\underline{s}$ $\{s_i; i = 1, ..., M\}$. As described in Section 1.4 the probability of each s_i is represented by a Gaussian:

$$P_i = \frac{1}{\sigma_i 2\pi} e^{-s_i^2/(2\sigma_i^2)} \tag{2.1}$$

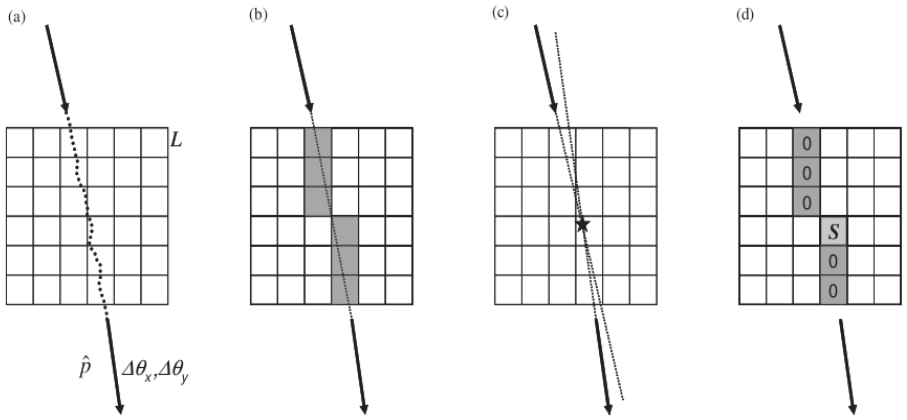

Figure 2.3: A 2D representation of the PCA algorithm: (a) muon's stochastic path through the volume; (b) estimate the muon path and identify through which the muon passed; (c) localize the PCA; (d) fill the PCA voxel with a signal value. [2]

where the variance σ_i^2 is related to the inverse of the radiation length $\lambda_0 = 1/X_0$ of the material by this line integral:

$$\sigma_i^2 = \frac{C}{p_i^2} \int_{path\ i} \lambda_0[r_i(\ell)]d\ell \tag{2.2}$$

where C is the constant seen in Equation 1.7 (C = 13.6^2 MeV^2), p_i is the momentum of the i-th muon and $r_i(\ell)$ is the parametric representation of the i-th path. So far the algorithm sets p_i as the average muon momentum (1 GeV); one of the aim of my project is to insert muon momentum information in this algorithm, which should improve the image quality and shorten the exposure time needed.
In order to evaluate this parametrization we need to use a M×N matrix, $\underline{\underline{L}}$, where M is the number of tracks and N is the number of voxels, and re-write:

$$\sigma_i^2 = (\underline{\underline{L}} \cdot \underline{\lambda})_i + \epsilon_i^2 = \sum_{j=1}^{N} L_{ij}\lambda_j + \epsilon_i^2 (i = 1, ..., M) \tag{2.3}$$

where ϵ_i is the experimental error on s_i that has been added in quadrature and L_{ij} is the product of C/p_i^2 times the path length of the i-th track through the j-th voxel (L_{ij} is set to zero for voxel not traversed by muons).
The problem of finding the most probable set of $\underline{\lambda}$ is solved with a Maximum Likelihood

Expectation Maximization strategy [12], i.e. finding the minimum of this function:

$$\psi(\underline{\lambda}) = \sum_{i=1}^{M} \left[\frac{s_i^2}{\sigma_i^2(\underline{\lambda})} + \ln(\sigma_i^2(\underline{\lambda})) \right] = \sum_{i=1}^{M} \left[\frac{s_i^2}{(\underline{\underline{L}} \cdot \underline{\lambda})_i + \epsilon_i^2} + \ln\left((\underline{\underline{L}} \cdot \underline{\lambda})_i + \epsilon_i^2 \right) \right] \tag{2.4}$$

The gradient is then easily evaluated as:

$$(\underline{\nabla}\psi)_j = \sum_{i=1}^{M} L_{ij} \frac{(\underline{\underline{L}} \cdot \underline{\lambda})_i + \epsilon_i^2 - s_i^2}{\left[(\underline{\underline{L}} \cdot \underline{\lambda})_i + \epsilon_i^2 \right]^2} \tag{2.5}$$

The iterations start with the scattering density $\underline{\lambda^{(0)}}$ equal to the inverse of the scattering length of air ($\lambda_i^{(0)} = 1/(3.039 \times 10^5$ mm) [18]); ψ and $\underline{\nabla}\psi$ are evaluated, and we look for the α value that minimizes:

$$\psi(\underline{\lambda^{(0)}} - \alpha \underline{\nabla}\psi) \tag{2.6}$$

At each iteration, the value of $\underline{\lambda}$ is updated as follows:

$$\underline{\lambda}^n = \underline{\lambda}^{n-1} - \alpha \underline{\nabla}\psi \tag{2.7}$$

where n is an integer from 1 to the number of iterations needed. After a number of iterations, the algorithm converges to the final $\underline{\lambda}$ which is used to fill the voxels in which the muon pass. This enables to produce the 3D image of the detected volume and distinguish the different materials within it.

2.4.5 Image quality

When trying to improve an algorithm, it is important to check these improvements. For this reason it is possible to evaluate the image quality of the tomographic pictures produced and see if adding information or changing the code would improve or otherwise.
In this stage it is possible to evaluate a Figure of Merit thanks to the true variable of the Monte Carlo simulation. The FoM is defined as the average *signal* minus the average *background* over the RMS of the *background* distribution:

$$\text{FoM} = \frac{\text{S} - \text{B}}{\sigma_{\text{B}}} \tag{2.8}$$

This time the word *signal* indicates the distribution of λ in the voxels in the target volume (e.g. an uranium sphere of 10 cm radius), and the word *background* indicates distribution

of λ in the volume of the container around the target.
The meaning of the Figure of Merit is understood looking at Figure 2.4(a): we want to see if some events in the signal region can be misunderstood as background, i.e. the high dense material is not distinguished by the environment. If the width of the background distribution reaches the mean of the signal distribution the high Z material could not be detected; otherwise the more the two distribution are distant, the easier it is to distinguish the target from the background.
Figure 2.4(b) shows an example of the different values of the Figure of Merit in dependence of the exposure time: as we might expect, the quality of the image improves with time.

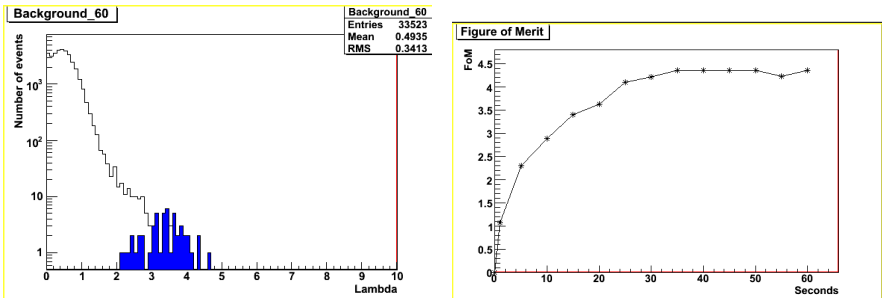

(a) (b)

Figure 2.4: (a) Distribution of the λ values of the signal (blue) and background (white) zones for an uranium sphere with 30 cm radius, with 60 seconds exposure time. (b) Example of Figure of Merit for different time exposures, in the case of an uranium sphere with 10 cm radius.

2.5 Results achieved with muon tomography

This new approach (using Multiple Coulomb Scattering) to the technique of the muon tomography has obtained very good results by different groups all around the World. Here I present some of the most interesting ones.

2.5.1 Image reconstruction and material discrimination by LANL

One of the first important results in this new approach of the muon radiography technique was achieved in 2004 by the Los Alamos National Laboratory (LANL). [2]
They introduced this new form of cosmic ray muon radiography based on the Multiple Coulomb Scattering. The experimental apparatus used was a small prototype as described

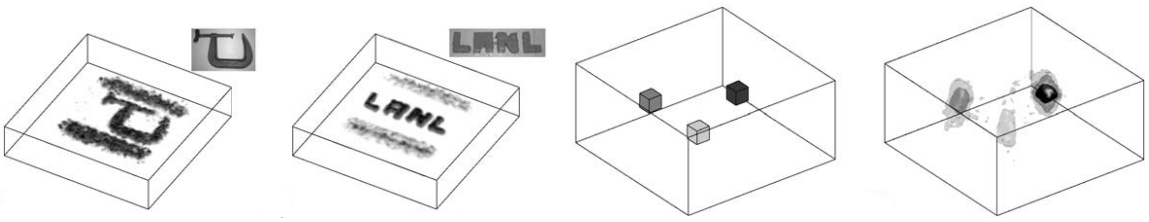

(a) (b)

Figure 2.5: (a) Two plots of experimentally produced muon radiography: a steel c-clamp on the left and the acronym LANL written with lead blocks on the right. (b) On the right there is the simulated muon radiography of the objects on the left: they are $5 \times 5 \times 5$ cm^3 cubes of tungsten (darkest), iron (less dark) and carbon (lightest). [2]

in Subsection 2.2; as regards the algorithms used for the data analyses, they introduced the Point of Closest Approach technique and they used a rough estimate of the muon momentum (obtained measuring the scattering of particles between plates of known material and thickness), but they did not use an iterative method to find the scattering density of the materials.
Figure 2.5(a) shows the radiographic images obtained with this new technique: in both pictures two lines appear above and below the target object, they are the steel beams that supported the objects. In the case of the steel c-clamp they are of the same intensity; it is clear then in the case of the lead bricks that the densities of the materials are different.
Figure 2.5(b) represents a Monte Carlo simulation of three $5 \times 5 \times 5$ cm^3 blocks of tungsten, iron and carbon; the reconstruction has been done using 100,000 muons, three additional iron plates of known thickness (for the momentum estimation) and the PCA algorithm.
This first experiment saw that this new approach enables to distinguish high and low Z materials, even though the technique needs to be improved to obtain higher quality images. See Reference [2] for a description in depth of this first achievement.

2.5.2 Material imaging with a large-volume muon tomography prototype by INFN

The Italian Institute of Nuclear Physics (*Istituto Nazionale di Fisica Nucleare*: INFN) published in 2009 an article describing their achievements in the muon tomography technique. [12]
The prototype used was very similar to the one described in Subsection 2.2, with the difference on the type of planes (they come from the CMS experiment at CERN [19]) and

the dimension of the inspected volume (11 m^3). The algorithms of track recognition and tomographic reconstruction are very similar to those of the CREAM TEA experiment, since part of them (e.g. the code which generates the $\underline{\lambda}$ values) have been improved thanks to the INFN work.
As a first test, the acronym INFN made by lead bricks was put into the prototype and its image has been reconstructed very clearly as seen in Figure 2.6(a).
Figure 2.6(b) shows the second step: two lead blocks on the left and two iron blocks on the right (with dimensions: $10 \times 10 \times 20$ cm^3) were placed on two shells with 65 cm of distance between lower and upper blocks.
Figure 2.6(c) represents five cubes of 10 cm side and one sample made staking two bricks of $10 \times 10 \times 4$ cm^3 (tungsten) of different materials which in order are brass, copper, lead, tungsten, iron and aluminium. The samples were arranged on a light support with a distance of 25 cm from each other.

From these images the success of this new approach of the muon tomography technique is clear: the probed volume has been mapped in its geometry very well, distinguishing the positions of the objects inside it; furthermore the difference between high and medium density material is evident.
Nevertheless, the discrimination between lead and denser material is difficult, due to the absorption of the low energy muons which biases the reconstruction of the scattering density ($\underline{\lambda}$). This means that measuring the muon momentum would improve the precision of these results.
For a deeper description of the experiment set up at the INFN see Reference [12].

2.5.3 Muon tomography by Department of Engineering Physics, Tsinghua University, Beijing

An important muon tomography improvement was achieved in 2009 by the Department of Engineering Physics of Tsinghua University in Beijing. [20]
Instead of the Maximum Likelihood Scattering (MLS) approach, described in Subsection 2.4.4 and used by both LANL and INFN, they used in their simulation the Maximum Likelihood Scattering and Displacement (MLSD) method. This improved algorithm takes into account not only the scattering deviation angle, but also the displacement between the incident track and the scattered track, as seen in Figure 2.7. Actually, they first solve the Maximum Likelihood with Expectation Maximization method (MLS-EM and MLSD-EM), as described in Subsection 2.4.4, and then used the initial values based on the Point

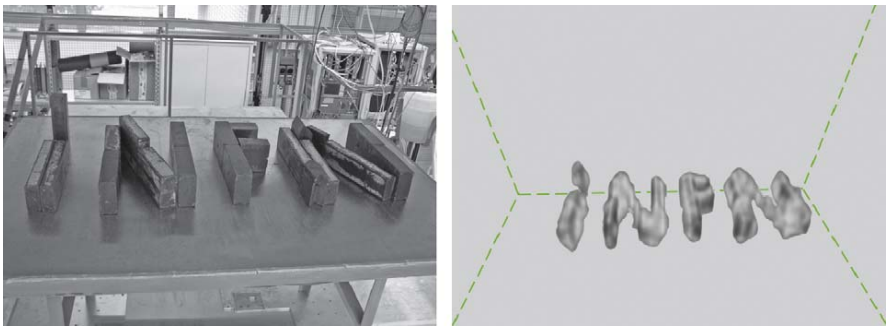

(a)

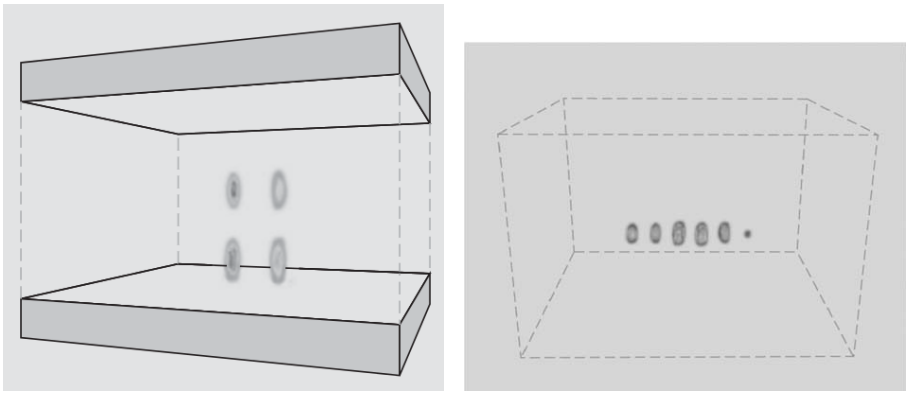

(b) (c)

Figure 2.6: (a) On the left hand side, the picture of the layout of the lead bricks; on the right the tomographic image obtained by INFN. (b) 3D view of the reconstructed image of two lead blocks on the left and two iron blocks on the right. (c) Image of six cubes; in order from the left: brass, Cu, Pb, W, Fe, Al. [12]

of Closest Approach in the EM method to use the Ordered Subsets (OS) technique and accelerate the reconstruction (MLS-OSEM and MLSD-OSEM).
Figure 2.8 shows two simulated layout and the results of performing different iterations and using the MLS-OSEM, MLSD-OSEM and MLSD-EM. It is clear from the picture that using the Ordered Subsets technique reduces the reconstruction time (we get a good quality image with less iterations). Furthermore, using the displacement information improve the image quality.
This means that adding information about the displacement even in the CREAM TEA experiment could potentially bring higher quality imaging.
For having more informations about this Chinese achievement see Reference [20].

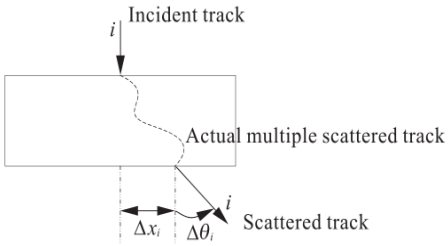

Figure 2.7: Representation of the scattering angle and displacement of a muon passing through a material [20]

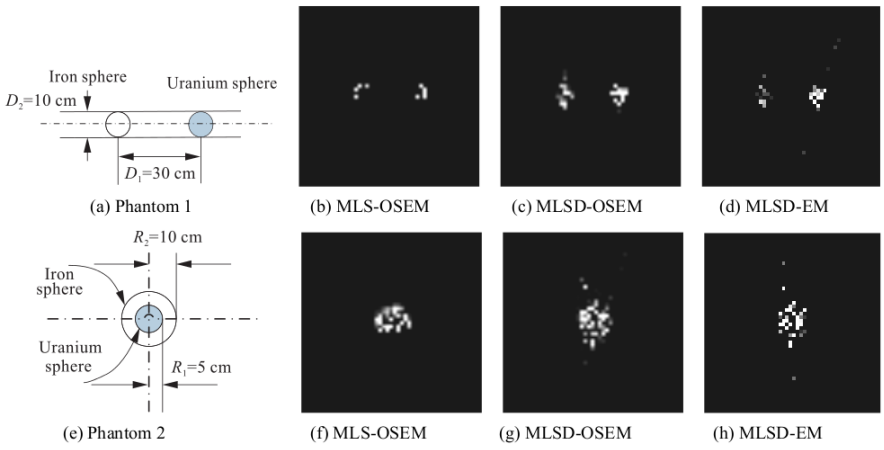

Figure 2.8: (a) Representation of Phantom 1, (b) MLS-OSEM, 20 iterations, Phantom 1, (c) MLSD-OSEM, 20 iterations,Phantom 1, (d) MLSD-EM, 60 iterations, Phantom 1, (e) Representation of Phantom 2, (f) MLS-OSEM, 20 iterations, Phantom 2, (g) MLSD-OSEM, 20 iterations, Phantom 2, (h) MLSD-EM, 60 iterations, Phantom 2

Part II

Coding improvements

Chapter 3

Muon momentum estimation

In this chapter I am going to explain the work done during this year to improve the reconstruction algorithm used by the CREAM TEA experiment.
So far the code uses a constant energy estimation for every muon (1 GeV): here, we will see the advantages of having a muon momentum estimation and how this can be performed.

3.1 Why is the muon estimation important?

In this phase I am modifying the reconstruction algorithm which is based on a paper written by the INFN in 2009 [12]. This code takes the information from the PCA (i.e. Point of Closest Approach, see Subsection 2.4.3 for further information), divides the probed volume (13 m $\times$ 13 m $\times$ 13 m) in 10^6 voxels (i.e. 3D pixels) and evaluates λ, the inverse of the radiation length, see Section 1.4 or Ref. [2]. The outputs of this algorithm are rootfiles which contain 2D slices of the probed volume.
In order to reconstruct the value of λ in each voxel, it is necessary to know the energy of the muon passing through it, as seen in Equation 1.7. The algorithm uses 1 GeV energy for every muon.
However, the spectrum of the cosmic ray muon momentum is broad, as seen in Figure 1.1, and it goes from 0.1 to 100 GeV approximately, with an average around 2-3 GeV. Hence, it is important to know at least the order of magnitude of the muon energy.
The first control is done to see if we can actually have an improvement by adding the energy information, and if so, what is its size. In Figure 3.1 we can see the two curves of the Figure of Merit (evaluated as described in Subsection 2.4.5): the black circles represent the true energy curve and the white squares represent the constant energy curve.

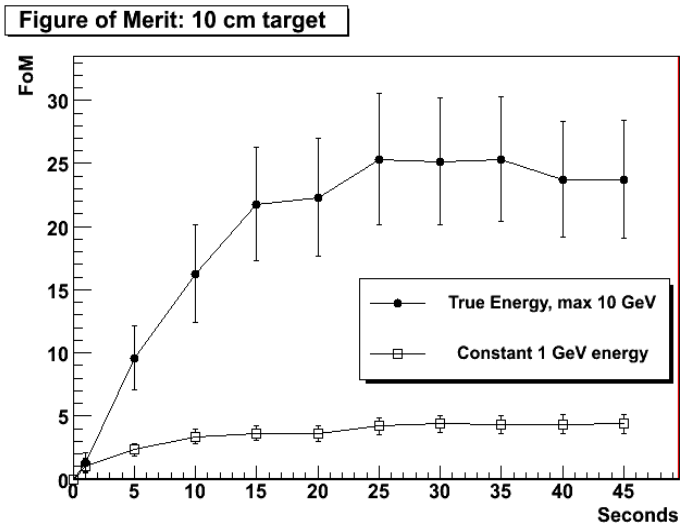

Figure 3.1: Curves of the FoM at different periods of exposure, using a constant muon energy of 1 GeV (□) and true Energy at 10 GeV threshold (•).

The improvement is clearly evident from 5 seconds muon exposure onwards (each second corresponds roughly to 28000 muons), where the FoM for the true energy is four times the FoM for the constant energy. The plot shows clearly the importance of having an estimation of the muon momentum.
In the same Figure, we can see that the error bars for the true energy are bigger than the ones for the constant energy. This is due to the presence of misleading voxels with high λ valuewhich is explained in Section 3.3, together with the necessity of having a threshold in the true energy, which in this case is 10 GeV.
Moreover, we can see in Figure 3.2, the difference between two slices: one reconstructed using the true energy and the other one using the constant energy. Both slices describe the same situation: a 10 cm radius uranium sphere inside a container. In the case of the constant energy the background inside the container is higher, making it more difficult to distinguish the target from the background. In the true energy plot it is easier to distinguish the target inside the container from the walls of the container; as we said above it is possible to see some voxels with a medium λ value.

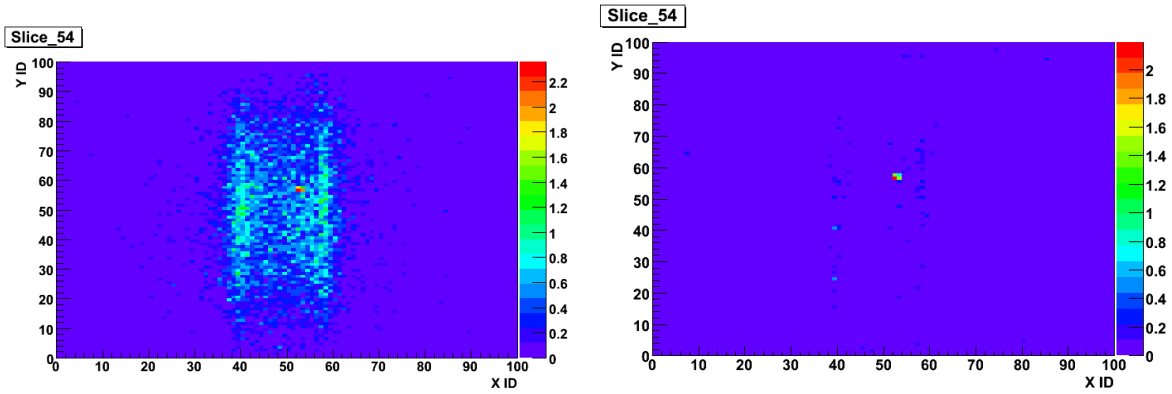

(a) (b)

Figure 3.2: Slices at z = 0.54 m of 10 cm uranium sphere positioned at (0.5, 1, 0.5) in steel container (2.44 m × 12.15 m × 2.59 m) with 20 seconds muon exposure: (a) Reconstructed image evaluated with a constant energy of 1 GeV; (b) Reconstructed image evaluated with the true energy with 10 GeV threshold.

3.2 How well should we measure the muon energy?

Now that we have demonstrated the importance of measuring the muon energy, we need to understand how precise our measurement must be in order to have good results.
This time instead of the true energy I used a generated random value within a Gaussian with the true energy as mean and different widths (10%, 20%, 30%, 40% and 50%), taking care that the energy is positive and smaller than 10 GeV.
Figure 3.3(a) shows the curves of the FoM for the two most significant situations: • represents the curve of the true energy with 10 GeV threshold, □ represents the curve of constant 1 GeV energy, ∘ represents the Gaussian with true energy as mean and 30% width; ∗ represents the Gaussian with true energy as mean and 50% width.
As it is clear in the picture, the curves generated using the Gaussian with 30% and 50% width are within the the error bars of the curve evaluated with the true energy at 10 GeV threshold.
This means that we do not need a high precision measurement: distinguishing between high energy (above 10 GeV) and medium energy (1-10 GeV) and low energy (0.1-1 GeV) muons will be sufficient to achieve an important improvement in our results.
However, Figure 3.3(a) shows that in the case of the Gaussian with 50% width, the method is not converging for 40 seconds exposure time (even after increasing the number of iterations performed). This happens because we are using the Expectation Maximisation

technique (as explained in Ref. [12]) that requires a minimisation of a cost function (see Equation 2.4) which depends on the muon energy and is summed over all the muons which pass through a voxel and then over all the voxels. In increasing the exposure time, we increase the number of muons; if our way of measuring the energy is fluctuating too much, the minimisation of this function gets impossible.
However, we do not need to be too concerned about this feature, since we get a good image of the probed volume from 20 seconds onwards as shown in Figure 3.3(c) which is very similar to Figure 3.2(b), apart from a few more voxels with a misleading λ value.
The value of the Figure of Merit does not change significantly between the Gaussian with different sigmas as shown in Figure 3.3(b) for a 10 cm target at 10 seconds muon exposure.

3.3 Which muon energy creates more problems?

In Section 3.1 we have seen that taking the true energy without putting a threshold can lead to a misleading estimation of the scattering density in some voxels. For this reason, it was necessary to research the best energy threshold.
The statistics we used relies on the fact that the central 98% of cosmic ray muons coming to Earth can be described by a Gaussian probability distribution [13] (see Section 1.4). The other 2% of muons have a very large scattering angle and do not follow the Gaussian. When evaluating the scattering density we need to minimise the cost function of Equation 2.4 which depends on the square of λ (which in turns depends on the scattering angle). If using a constant estimation of energy, the influence of these 2% muons on the cost function is negligible, but when using the true energy sometimes a high energy muon combined with a large scattering angle makes the cost function difficult to minimise to the correct value. The presence of these disturbed voxels can make the detection of high Z material misleading, for this reason when considering the true energy we need to put a threshold (these misleading voxels make the error bars in Figure 3.1 bigger in the true energy case than in the constant energy case).
The research for the best threshold has been performed by setting a threshold E_0 and then using:

- true energy E, if $E < E_0$;
- constant energy E_0, if $E > E_0$.

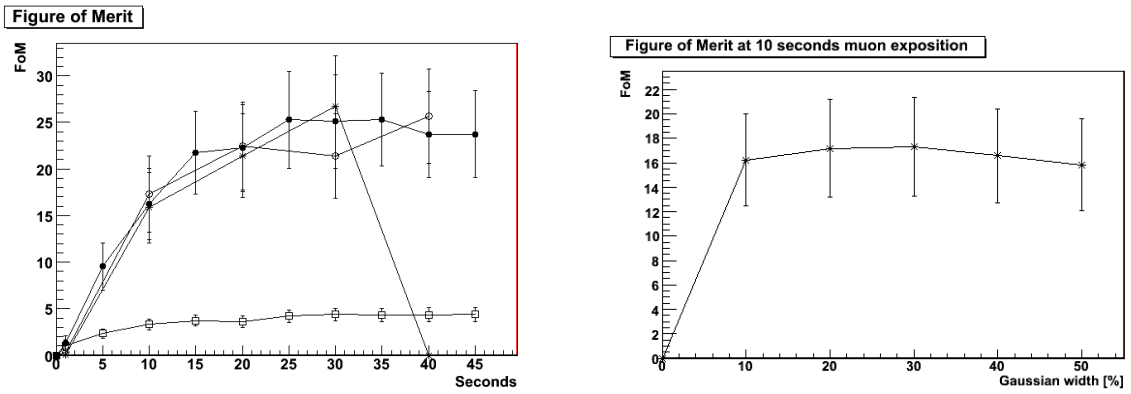

(a) (b)

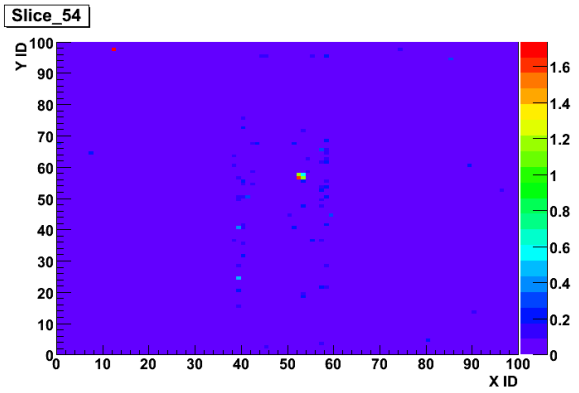

(c)

Figure 3.3: (a) Curves of the FoM for 10 cm target: • true Energy with 10 GeV threshold, □ constant 1 GeV energy, ∘ Gaussian with true energy as mean and 30% width; ∗ Gaussian with true energy as mean and 50% width; (b) Figures of Merit for 10 cm target at 10 seconds exposure and Gaussian with sigma equal to 10%, 20%, 30%, 40% and 50%. (c) Slice at z = 0.54 m of 10 cm uranium sphere positioned at (0.5, 1, 0.5) in steel container of 2.44 m × 12.15 m × 2.59 m with 20 seconds muon exposure, reconstructed image evaluated with Gaussian of true energy as mean and 50% sigma.

Figure 3.4(a) shows the curves for the FoM in the case of constant 1 GeV energy (□), true energy without threshold (○), true energy with 10 GeV threshold (●) and true energy with 2 GeV threshold (△). The plot clearly shows that using the true energy without any threshold is not convenient. This is reinforced even by Figure 3.4(c) which shows a slice of 10 cm uranium sphere inside a truck at 20 seconds exposure time. The presence of many voxels with a high scattering density is evident and this leads to a higher background and a more difficult detection of the uranium inside the truck.
Figure 3.4(b) shows that the value of the FoM at constant time of exposure (10 seconds) changes just slightly from 1 GeV threshold to 10 GeV threshold. This means that we only need to measure precisely (as described in Section 3.2 low energy muons.
Unfortunately, the algorithm is not converging in the case of 1 GeV threshold for time exposure higher than 10 seconds. For this reason Figure 3.4(a) shows the curve of the Figure of Merit for a 2 GeV threshold. This curve lies in the error bars of a 10 GeV threshold and underlines the fact that having a rough estimation of the momentum of low energy muons will improve our results considerably.
Moreover, Figure 3.4(d) shows a slice of the 10 cm uranium sphere in a truck, obtained with a 2 GeV threshold at 20 seconds exposure time. The image of the target is clearer than in Figure 3.4(c) without a threshold, and it is comparable to Figure 3.2(b) with a 10 GeV threshold.
Even though the quality of the image changes just slightly from a 2 GeV to a 10 GeV threshold (as shown in Figure 3.4(b)) the choice of using a 10 GeV threshold for the ideal situation of measuring the true energy is due to the muons momentum distribution:

- $E < 1$ GeV : 33.71 %;
- $E < 5$ GeV : 93.72 %;
- $E < 10$ GeV : 98.62 %.

3.4 How can we evaluate the muon momentum?

Unfortunately measuring the muon energy is not an easy task. For this reason I tried different ways of estimating this energy to see which one produced the best result.

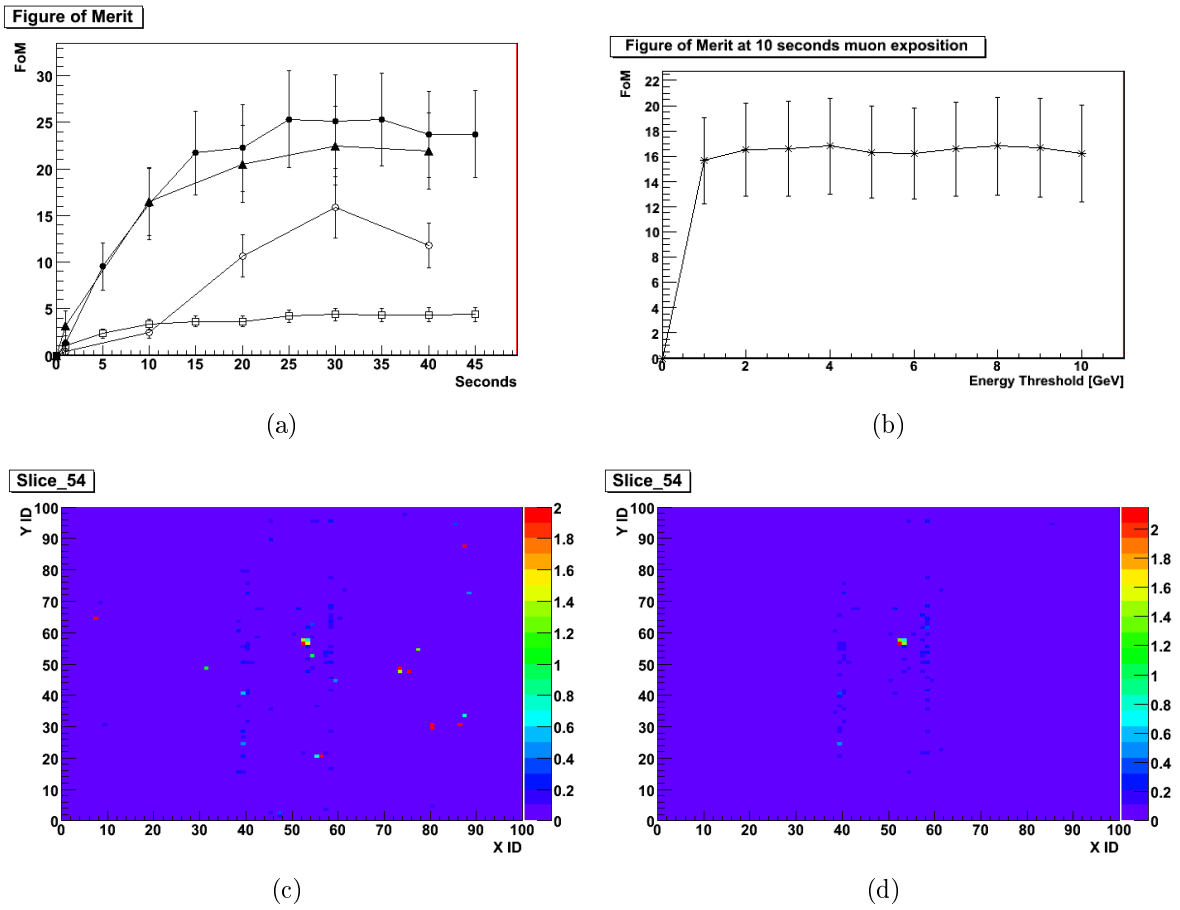

Figure 3.4: (a) Curves of the Figure of Merit for 10 cm target: • true Energy with a 10 GeV threshold, □ constant 1 GeV energy, △ true Energy with a 2 GeV threshold; ∘ true Energy without a threshold; (b) Figures of Merit for 10 cm target at 10 seconds exposure and Gaussian with a threshold at 1, 2, 3, 4, 5, 6, 7, 8, 9 and 10 GeV; (c) Slice at z = 0.54 m of 10 cm uranium sphere positioned at (0.5, 1, 0.5) in steel container of 2.44 m × 12.15 m × 2.59 m with 20 seconds muon exposure, reconstructed image evaluated with true energy without a threshold; (d) Slice at z = 0.54 m of 10 cm uranium sphere positioned at (0.5, 1, 0.5) in steel container of 2.44 m × 12.15 m × 2.59 m with 20 seconds muon exposure, reconstructed image evaluated with true energy with a 2 GeV threshold.

E $[GeV]$	γ	β	T_1 [s]	T_2 [s]	T_3 [s]	T_4 [s]
1	9.4645	0.9940	$6.7088\ 10^{-11}$	$3.3544\ 10^{-9}$	$4.3607\ 10^{-8}$	$5.0316\ 10^{-8}$
10	94.645	0.99994	$6.6717\ 10^{-11}$	$3.3358\ 10^{-9}$	$4.3366\ 10^{-8}$	$5.0037\ 10^{-8}$
100	946.45	0.9999994	$6.6713\ 10^{-11}$	$3.3356\ 10^{-9}$	$4.3363\ 10^{-8}$	$5.0035\ 10^{-8}$
		ΔT 1-10 GeV	$3.71\ 10^{-13}$	$1.84\ 10^{-11}$	$2.42\ 10^{-10}$	$2.79\ 10^{-10}$

Table 3.1: Times of flight of muons with different energy (1, 10, 100 GeV) through different path lengths.

3.4.1 Looking at the time of flight

The first question we need to answer is: what is the time resolution for the detector to distinguish a 1 GeV muon from a 10 GeV muon?
The answer is a little straight forward math, recalling Einstein relation $E = m\gamma c^2$ and $\gamma = \frac{1}{\sqrt{1-\beta^2}}$. Table 3.1 shows the summary of the times of flight of muons with different energies (1, 10 and 100 GeV) through different path:

1. $T_1 \rightarrow \Delta x = 0.02$ m : approximate thickness of one scintillator plane;
2. $T_2 \rightarrow \Delta x = 1$ m : approximate thickness of the set of scintillator planes above and below the detected volume;
3. $T_3 \rightarrow \Delta x = 13$ m : height of the probed volume;
4. $T_4 \rightarrow \Delta x = 15$ m : approximate distance from the first scintillator plane above the detected volume and the last plane below it.

ΔT in Table 3.1 represents the difference in the time of flight between a 1 GeV muon and a 10 GeV muon. For distinguishing these two muons considering just the path inside a plane, the time precision should be on the scale of 0.1 picoseconds. Measuring the time of flight between the first and the last plane of the same set of scintillator planes (above or below the probed volume) would require a time resolution of around 10 picoseconds. The best situation possible to achieve this is to measure the time of flights between the first scintillator plane of the above detector and the last scintillator plane of the below detector. Distinguishing a 1 GeV muon from a 10 GeV muon in this case would require a precision of the order of 100 picoseconds.

3.4.2 Looking at the mean energy above and below a threshold

Measuring the times of flight is not easily achievable, since a precision of about 0.1 nanoseconds is necessary. What can easily be done is to put a kind of "veto" under the lower detector: all the muons with energy above a given threshold will pass the veto, all the others will not. In this way we can set a mean energy for muons above and below this threshold and improve the quality of our measurements.
The simulations have been run with these parameters:

- $E_0 = 5$ GeV : $< E >_{BELOW} = 1.6$ GeV, $< E >_{ABOVE} = 8.5$ GeV;
- $E_0 = 4$ GeV : $< E >_{BELOW} = 1.4$ GeV, $< E >_{ABOVE} = 6.9$ GeV;
- $E_0 = 3$ GeV : $< E >_{BELOW} = 1.3$ GeV, $< E >_{ABOVE} = 5.4$ GeV;
- $E_0 = 2$ GeV : $< E >_{BELOW} = 1$ GeV, $< E >_{ABOVE} = 4$ GeV;
- $E_0 = 1.5$ GeV : $< E >_{BELOW} = 0.8$ GeV, $< E >_{ABOVE} = 3.4$ GeV;
- $E_0 = 1.25$ GeV : $< E >_{BELOW} = 0.7$ GeV, $< E >_{ABOVE} = 3$ GeV;
- $E_0 = 1$ GeV : $< E >_{BELOW} = 0.6$ GeV, $< E >_{ABOVE} = 2.7$ GeV;

The cases of $E_0 = 5$ GeV, $E_0 = 4$ GeV and $E_0 = 3$ GeV produce slices very similar to the constant energy images; hence, the curves of their FoM are close to the constant energy curves.
In the case of $E_0 = 1$ GeV the algorithm does not find the minimum of the cost function, since the energies are too roughly estimated.
Figure 3.5(a) shows the curves of the FoM in the case of $E_0 = 2$ GeV, $E_0 = 1.25$ GeV and the usual true energy and constant energy curves. The plot emphasizes that this rough method of estimating energy can achieve a significant improvement in the image quality. The curve of $E_0 = 1.25$ GeV appears to be the best way of measuring the energy so far.
Figure 3.5(b) shows the Slice at z = 0.54 m of a 10 cm uranium target in the case of 1.25 GeV border line and 20 seconds time exposure. If we compare this plot to the one evaluated with the true energy (Figure 3.2(b))), we can see that they are very similar, although in this one there are more "background" voxels.
This method of dividing the muons above and below a threshold could be easily achieved and represents a significant improvement.

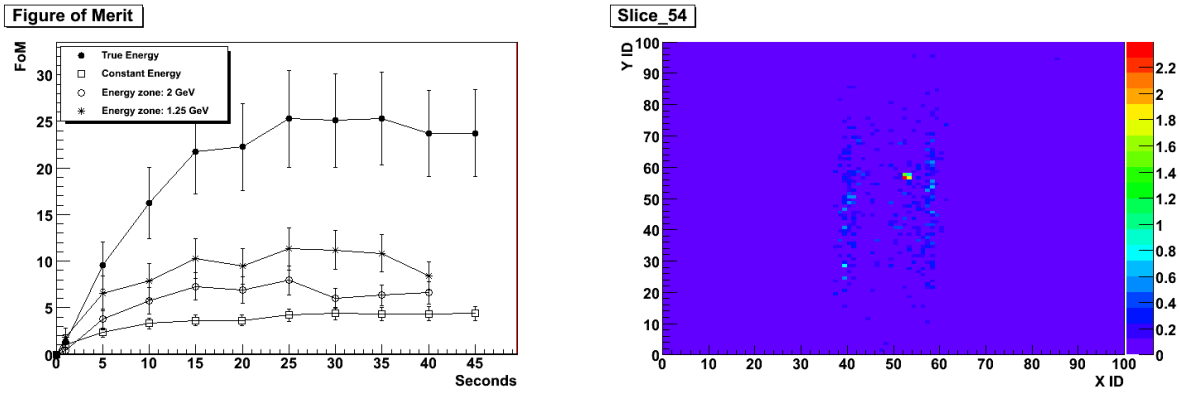

(a) (b)

Figure 3.5: (a) Curves of the FoM in the case of: • true Energy with 10 GeV threshold, □ constant 1 GeV energy, ∘ Energy zone: $E_0 = 2$ GeV ; ∗ Energy zone: $E_0 = 1.25$ GeV . (b) Slice at z = 0.54 m of 10 cm uranium sphere positioned at (0.5, 1, 0.5) in steel container of 2.44 m × 12.15 m × 2.59 m with 20 seconds muon exposure, reconstructed image evaluated with Energy zone: $E_0 = 1.25$ GeV.

3.4.3 Looking at the energy deposited by muons in each strip

The detector we are using in our simulations is composed of 8 scintillator planes above and below the probed volume. Each scintillator plane is divided into strips as the kind in the MINERvA experiment [15], i.e. with the shape of a toblerone (see Subsection 2.3.1).
Muons passing through the volume leave some energy in the strips which is used to reconstruct the trajectory of the muons before and after traversing the probed volume. This energy deposit divided by the path of the muon inside the strip is related to the muon momentum (as described in Section 1.3). Measuring the mean and the RMS of the energy deposit over the length of the path, it is possible to obtain an estimation of the muon momentum.
First of all, I have written a simple function to evaluate the path of muons inside a strip and that is explained in Appendix A.
Then I have checked that the results found with this function were reasonable and this is shown in Figure 3.6(a) in which the x axis represents the path length of the muon inside the strip in mm, the y axis represents the energy deposited by muons in the strip in MeV, and the z axis the number of events with these characteristics. The proportionality between the path length and the energy deposit is reasonable, thus we can consider our method to estimate the muon momentum reasonable.
The next step was to create a plot with the mean and RMS of the energy deposit over

the path length ($\frac{dE}{dx}$) with the average true energy on the z axis and this is shown in Figure 3.6(b). As it is possible to see the plot is uniform, and using this plot to have an estimation of the muon energy does not produce an important improvement, since we end up with an average constant energy between 2 GeV and 3 GeV for all muons. This is well highlighted by Figure 3.6(c) in which we see that our curve of the FoM with the energy evaluated in this method is close to the curve of the FoM evaluated with a constant energy. This happens because the three regions we want to distinguish in the energy spectrum (0-1 GeV, 1-10 GeV, 10-100 GeV) have a mean and a RMS of the $\frac{dE}{dx}$ almost in the same region with mean and RMS 0.1-0.2 MeV/mm. This is reasonable considering that the average energy deposit in each strip is around 2 MeV and the average path length of muons in the strip is around 20 mm (because most of the muons are coming with a small zenith angle and the plane width is 17 mm). This concept is underlined by Figures 3.6(d), 3.6(e) and 3.6(f), which shows that most of the muons have the same mean and RMS dE/dx regardless of energy.
Moreover, Figures 3.7(a) and 3.7(b) recall the shape of the curve of the mean energy loss of charged particles in Figure 1.2(b), but they show little correlation between the energy deposit and the muon energy. Hence, the energy deposit alone is not enough to reach a rough estimation of the muon energy.

3.4.4 Looking at the muon scattering inside the planes

Low energy muons passing through the scintillator planes interact with the detector and scatter inside the detector more than high energy muons.
During the evaluation of the Point of Closest Approach, we fit the positions of the strips hit by the muon with a straight line. In this fit we evaluate a "quality factor" which is the sum of the squared distance between the n-th point and the fitted line. This quality factor could be used to estimate muon energy, as underlined by Figures 3.8(a) and 3.8(b) which show a strong dependence in the energy at least between 0 and 5 GeV.
High energy muons tend to pass straight through in the detector and this factor should be very small (typically less than 0.1 for muons with energy above 2 GeV), vice versa low energy muons scatter more inside the detector and this factor is higher (around 0.5 for 1 GeV muons).
Figure 3.9(a) shows the plot used to evaluate the muon energy: the plot is more precise for medium low energy muons (less than 4 GeV) than for high energy muons. For this reason,

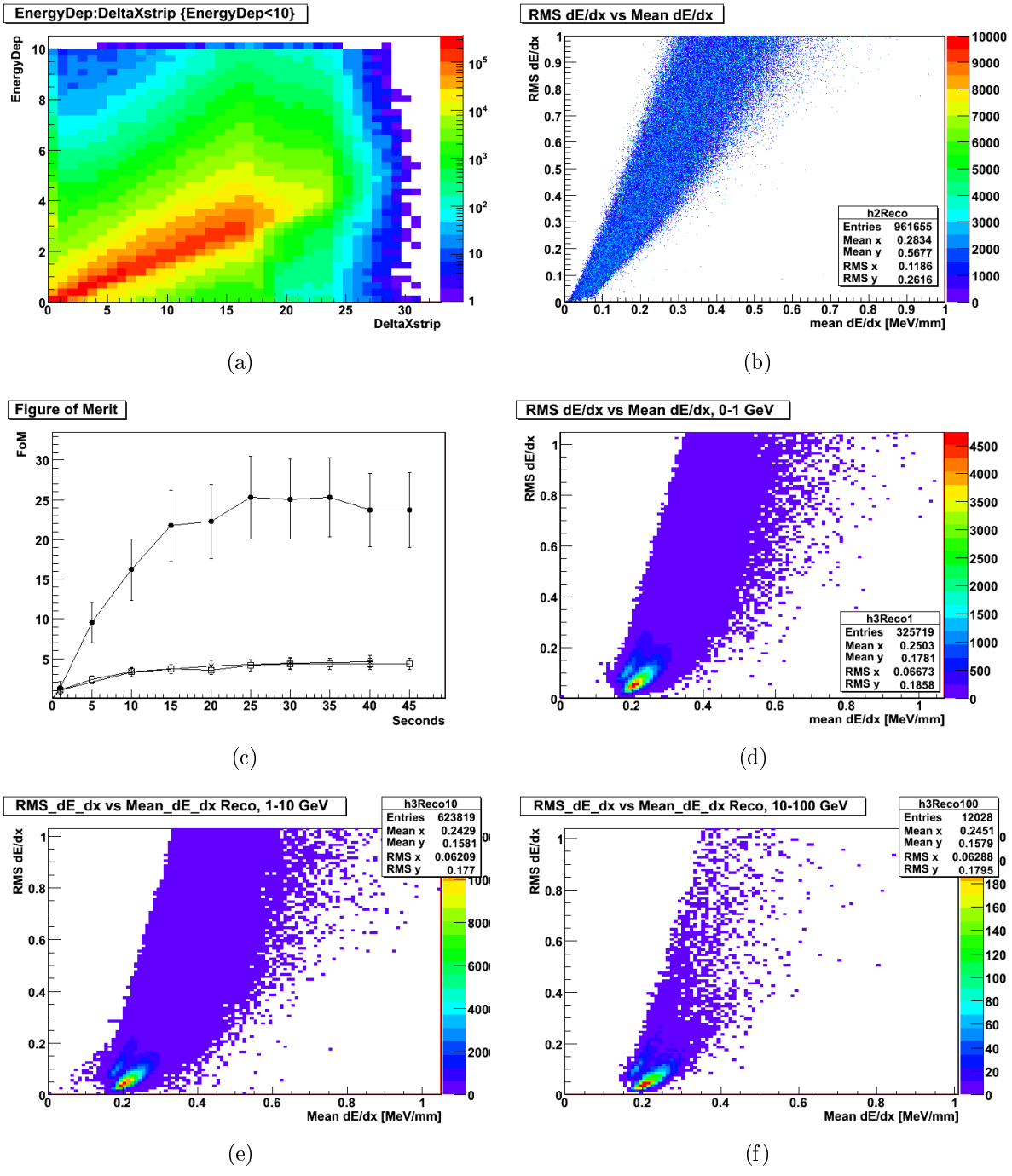

Figure 3.6: (a) Plot of dE/dx in MeV as a function of the path of the muon inside the strip; (b) Plot of mean vs RMS dE/dx with mean true energy on z axis in MeV. (c) Curves of the Figure of Merit for 10 cm uranium target with 20 seconds exposure: • true energy with 10 GeV threshold, □ constant 1 GeV energy, ∗ evaluated energy. (d), (e) and (f) Plots of mean vs RMS dE/dx with number of events on z axis in MeV with energy range $0 < E < 1$ GeV (d), $1 < E < 10$ GeV (e) and $10 < E < 100$ GeV (f).

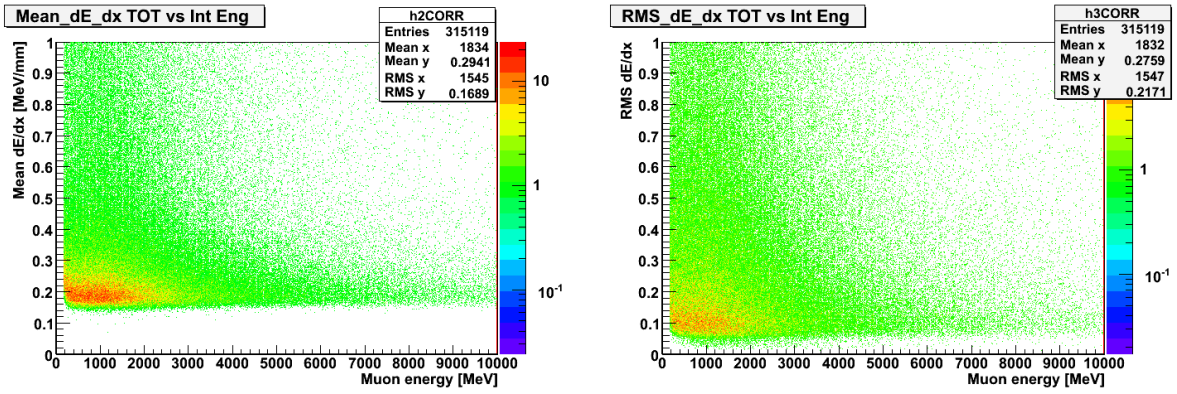

(a) (b)

Figure 3.7: (a) Plot of the mean energy deposit as a function of the muon energy. (b) Plot of the RMS energy deposit as a function of the muon energy.

I tried to combined this technique with the veto explained in Subsection 3.4.2, in the case of $E_0 = 3$, 4 and 5 GeV. Therefore, if the muon has an energy higher than the threshold E_0, it does not pass the veto and its energy is set to a constant value, otherwise its energy is evaluated with the fit quality parameters.
In Figure 3.8(b) we can see the curves of FoM evaluated with this method of energy estimation. When the threshold is 10 GeV, we measure the energy of 98.62 % (as seen in Section 3.3) of muons and we get a slightly improved quality image from the situation of the constant energy. The best improvement is given by the threshold at 5 GeV, combined with this method of evaluation of the energy.

3.4.5 Trying to build a likelihood

The next step is trying to use the information of the energy deposited in each strip and of the fit quality factor together in order to get a more precise evaluation of the energy. Actually, the information about the fit quality factor could help us better distinguish the information about the energy deposit and see more clearly if the latter could be useful or not.
The method used was simple in terms of derivation, but more expensive computationally (all the other methods inside the PCA algorithm take around 15 minutes to run in the cluster of UCL HEP computers, while this method took between 19 and 25 hours). Firstly, I built six 3D-histograms, weighted by the number of events, as:
For each event there are values of the 4 variables: A (Quality fit up), B (Quality fit down),

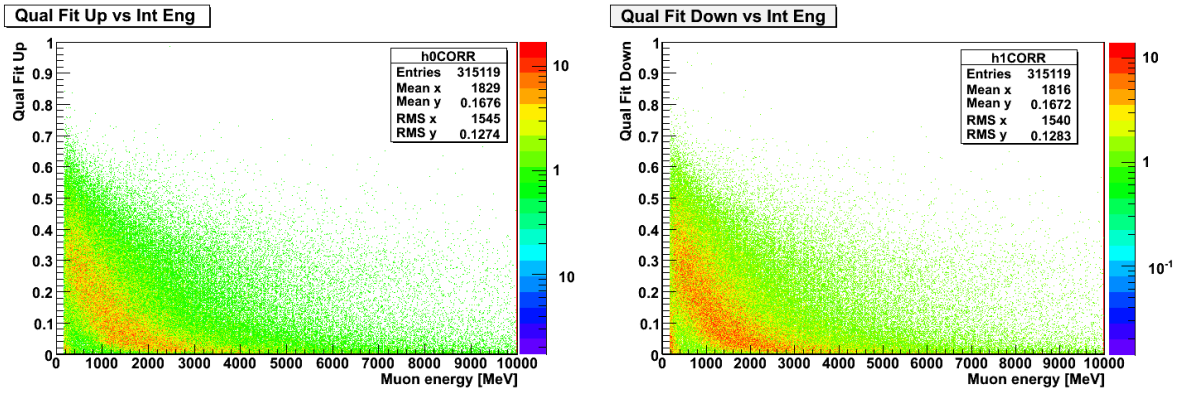

(a) (b)

Figure 3.8: (a) Plot of the fit quality factor for the above set of scintillator planes as a function of the muon energy. (b) Plot of the fit quality factor for the below set of scintillator planes as a function of the muon energy.

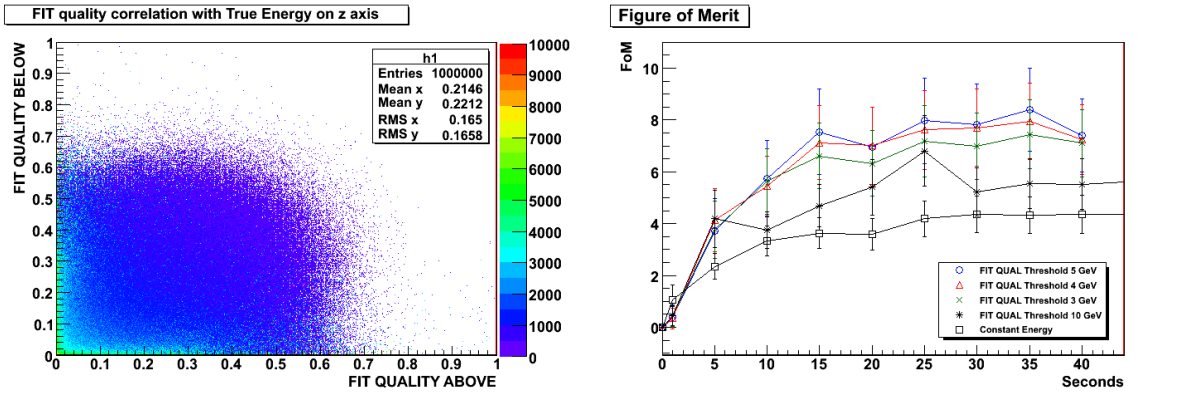

(a) (b)

Figure 3.9: (a) Plot of quality factor for above set of detectors on x axis, quality factor for below set of detectors on y axis, muon energy on z axis; (b) Curves of the Figure of Merit.

name	x axis	y axis	z axis
h1	Quality Fit Up	mean dE/dx	muon Energy
h2	Quality Fit Down	mean dE/dx	muon Energy
h3	Quality Fit Up	RMS dE/dx	muon Energy
h4	Quality Fit Down	RMS dE/dx	muon Energy
h5	Quality Fit Up	Quality Fit Down	muon Energy
h6	RMS dE/dx	mean dE/dx	muon Energy

C (mean dE/dx) and D (RMS dE/dx), and the procedure for each event is as follows:

1. Measure the values of A, B, C and D;
2. Take the projection on z axis of the histogram h1 in the point (A, B), to find the 1D histogram which is the distribution of energy corresponding to (A, B);
3. Normalise the projection with the number of events in that 1D histogram, to find the probability distribution h1-1D;
4. Repeat step 2 with (A, C) in h3, to find h3-1D;
5. Multiply h1-1D and h3-1D to find the joint probability distribution;
6. Fit the distribution with a Landau-Valivov function and get the maximum as the most probable energy value (alternatively, take the maximum of the distribution)

This procedure has been used in three cases:

1. (Fit Quality up, Fit Quality down) and (RMS dE/dx, Fit Quality up);
2. (Fit Quality up, Fit Quality down) and (mean dE/dx, Fit Quality up);
3. (Fit Quality up, Fit Quality down) and (mean dE/dx, RMS dE/dx);
4. (Fit Quality up, Fit Quality down), (mean dE/dx, Fit Quality up) and (RMS dE/dx, Fit Quality up);

Figure 3.10 shows the plots of the evaluated energy as a function of the true energy. Subfigure 3.10(a) clearly illustrates the proportionality between the evaluated energy and the true energy when using the fit quality method. Subfigures 3.10(b), 3.10(c) and 3.10(d) show that this method of taking the joint probability makes this plot worse. This means that instead of helping, the information of the energy deposit smoothes the probability

distribution to an average value. This concept is further underlined by Subfigure 3.10(e): using the two pieces of information on the energy deposit almost delete the information gained from the fit quality factor.
In this context, we can say that the energy deposited by the muons in each strip cannot give significant information about the muon energy.

3.5 What is the most convenient way of evaluating the muon energy?

In this chapter we have seen that measuring the muon energy can bring a significant improvement in the reconstruction algorithm. Moreover, it is necessary just to know the order of magnitude of the energy to improve the image quality (distinguishing between 0.1-1 GeV, 1-10 GeV and 10-100 GeV muons).
Unfortunately, measuring the time of flight is not feasible with the timing precision available in the CREAM TEA technology. Trying to use the information about the energy deposited by each muon in the strips is not sufficient to provide a acceptable estimation of the energy, since we end up with just an average.
A feasible and significant improvement can be achieved using an energy threshold at 1.25 GeV. Moreover, the fit quality factor managed to give a good estimation of medium low energy muons (less than 5 GeV).
A comparison of the two most significant methods tried can be found in Figure 3.11. The two curves of the evaluated energy are closely distributed such that their error bars overlap and both represent a little improvement from the constant energy curve. However, the curve evaluated just using the threshold at 1.25 GeV seems to be the best way to improve the quality of our images.

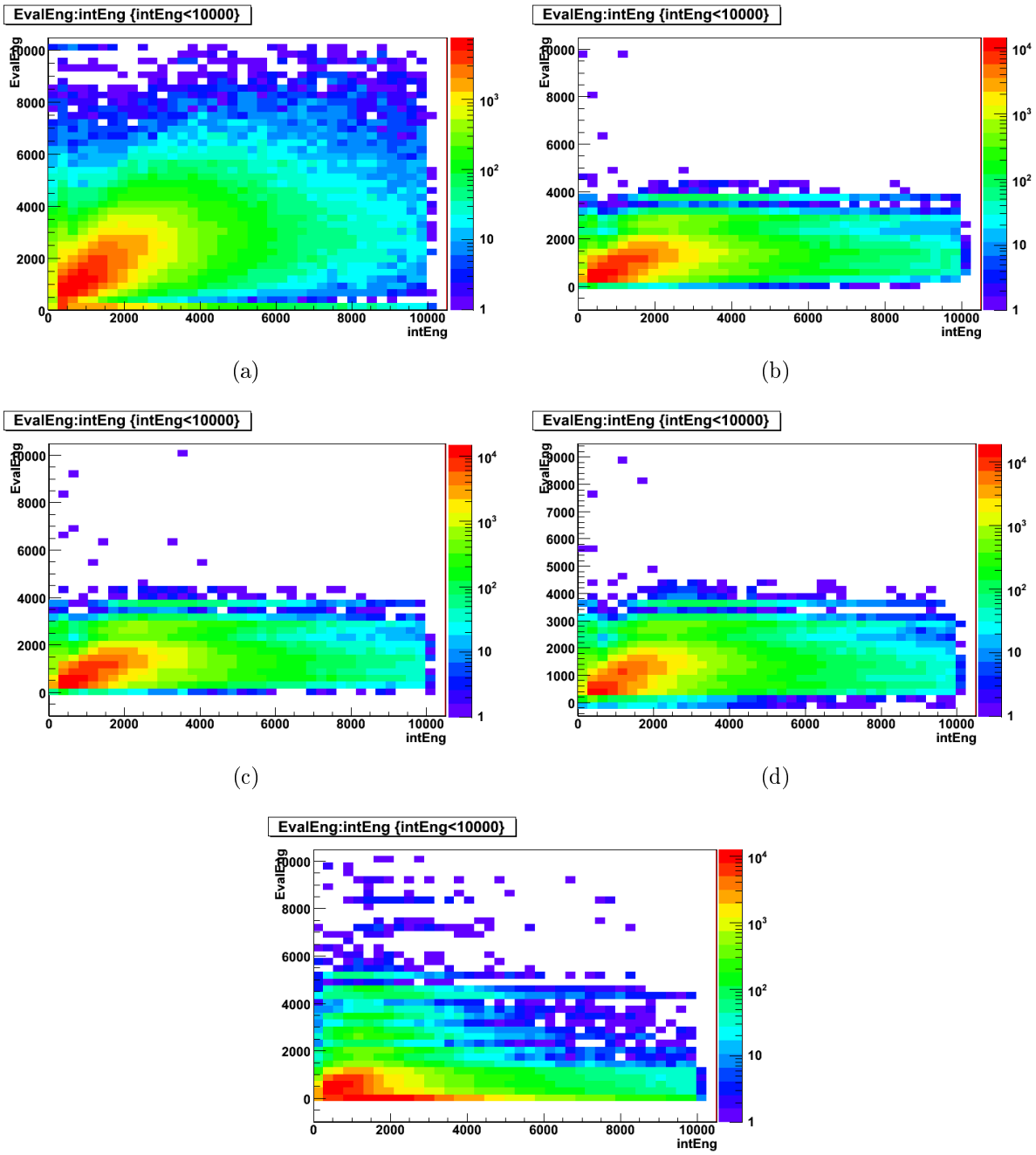

Figure 3.10: Plots of true Energy on the x axis, evaluated energy on the y axis and number of events on the z axis. Energy reconstructed using these plots: (a) (Fit Quality up, Fit Quality down); (b) (Fit Quality up, Fit Quality down) and (RMS dE/dx, Fit Quality up); (c) (Fit Quality up, Fit Quality down) and (mean dE/dx, Fit Quality up); (d) (Fit Quality up, Fit Quality down) and (mean dE/dx, RMS dE/dx); (e) (Fit Quality up, Fit Quality down), (mean dE/dx, Fit Quality up) and (RMS dE/dx, Fit Quality up).

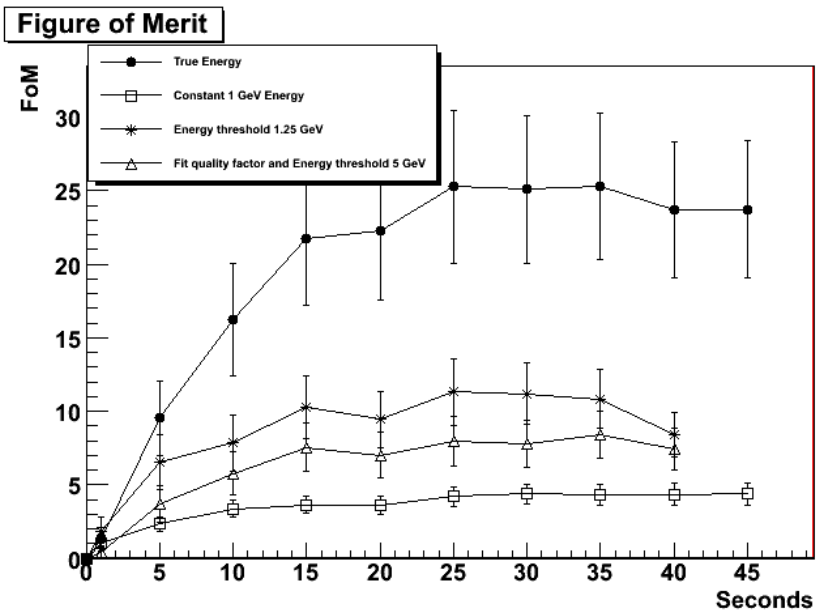

Figure 3.11: Curves of the FoM at different period of exposure, using a constant muon energy of 1 GeV (□), true Energy at 10 GeV threshold (•), energy threshold at 1.25 GeV (∗) and fit quality factor with 5 GeV threshold (△).

Chapter 4

Scattering and displacement

The reconstruction algorithm described in Subsection 2.4.4 is based on a paper written by the INFN in 2009 [12]. This code uses the Expectation Maximisation technique [21] with the muon scattering angle as input.
Other important works, such as the Chinese paper described in Subsection 2.5.3 and Ref. [20], suggest the possibility to use the displacement of the ray together with the scattering angle. This Chapter describes the Expectation Maximisation technique for scattering and displacement (Maximum Likelihood Scattering and Displacement, MLSD), as described in a previous work by LANL [13] and the improvements we can get using this technique.

4.1 Displacement evaluation

In Subsection 2.4.4 the reconstruction algorithm is described on the assumption that the 98% of central muons coming to Earth in the Multiple Coulomb Scattering follow a Gaussian distribution with zero as mean and RMS described by:

$$\sigma_\theta = \frac{13.6 \text{ MeV/c}}{p}\sqrt{\frac{x}{X_0}} \tag{4.1}$$

where x is the muon path through the material, X_0 is its radiation length and p is the muon momentum measured in MeV/c.
The CREAM TEA experiment uses an algorithm that tries to reconstruct the value of the inverse of the radiation length of the material, λ, and use it to create an image of the

probed volume:

$$\lambda(X_0) = \frac{1}{X_0} \tag{4.2}$$

It is clear that the root mean square of the scattering angle is related to this λ of the material as follows:

$$\sigma_\theta^2 = \left(\frac{13.6}{p}\right)^2 \lambda x = p_r^2 \lambda x \tag{4.3}$$

where $p_r = \dfrac{13.6}{p}$ is a factor which takes into account the muon momentum.
The displacement Δx and the scattering angle $\Delta\theta$ are correlated. Their distribution can be described as a jointly Gaussian [8] with zero mean and:

$$\sigma_{\Delta x} = \frac{x}{\sqrt{3}} \sigma_{\Delta\theta} \tag{4.4}$$

$$\rho_{\Delta\theta\Delta x} = \frac{\sqrt{3}}{2} \tag{4.5}$$

Moreover, the covariance matrix can be expressed as follows:

$$\Sigma \equiv \begin{bmatrix} \sigma_{\Delta\theta}^2 & \sigma_{\Delta\theta\Delta x} \\ \sigma_{\Delta\theta\Delta x} & \sigma_{\Delta x}^2 \end{bmatrix} = \left(\frac{13.6}{p}\right)^2 \lambda \begin{bmatrix} x & x^2/2 \\ x^2/2 & x^3/3 \end{bmatrix} \tag{4.6}$$

For simplicity, we can define the matrix A as:

$$A = \begin{bmatrix} x & x^2/2 \\ x^2/2 & x^3/3 \end{bmatrix} \tag{4.7}$$

and write Equation 4.6 as:

$$\Sigma = \left(\frac{13.6}{p}\right)^2 \lambda A \tag{4.8}$$

In three dimensions, we may consider scattering in two orthogonal planes, referring to scattering angles $\Delta\theta_x$ and $\Delta\theta_y$ and displacements Δx and Δy. Deflections into x and y plane are independent and identically distributed, as seen in Ref. [8].
For this reason, we can proceed considering a system oriented orthogonally to the direction of the incident muon and see the projections of the displacements and angles. Figure 4.1 shows a muon incident at a projected angle θ_{x0} and scattered at a projected angle θ_{x1} with displacement Δx (a similar situation would occur on the yz plane).

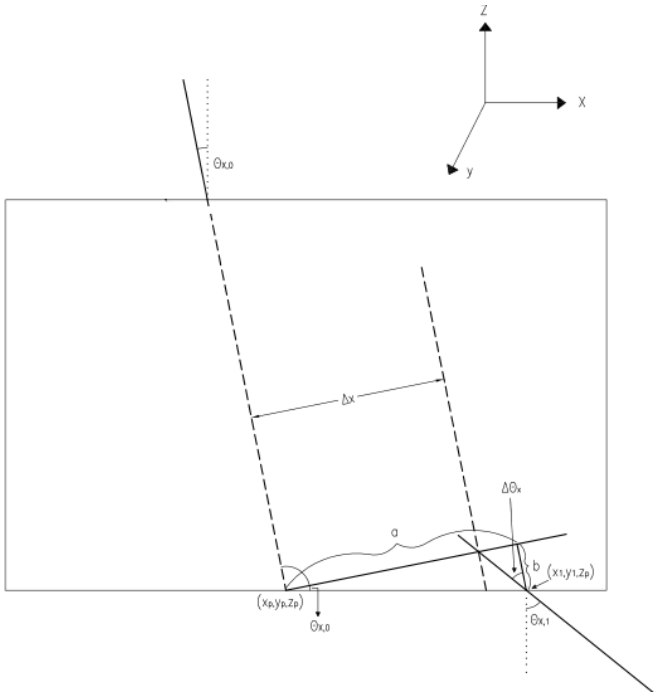

Figure 4.1: Projection of the muon path inside the probed volume and definition of scattering displacement.

The scattering angle is defined as:

$$\Delta\theta_x = \theta_{x1} - \theta_{x0} \tag{4.9}$$

and the displacement as:

$$\Delta x = \Delta x_m \frac{\cos(\Delta\theta_x + \theta_{x0})}{\cos\Delta\theta_x} \cos\theta_{x0} L_{xy} \tag{4.10}$$

where the angles are the same as in Figure 4.1, $\Delta x_m = x_1 - x_p$ and the definition of L_{xy} is given in Section B.1, together with the derivation of this formula.
The procedure for the Maximum Likelihood Expectation Maximisation reconstruction in this case follows the same steps as described in Section 2.4.4, but starting from a probability which takes into account both scattering and displacement. Details of this procedure can be found in Ref. [13] and [22] or in Section B.3.

4.2 Maximum Likelihood Scattering and Displacement

The first step was reproducing the exact algorithm described in Ref. [13] which relies on the Maximum Likelihood for Scattering and Displacement (MLSD) technique, explained in Section B.3.
The procedure used is summarised in 6 steps:

1. Gather measurements of scattering angles, displacements and momentum for each muon $i = 1$ to M: $(\Delta\theta_x, \Delta\theta_y, \Delta x, \Delta y, p)_i$;

2. Estimate the geometry of interaction of each muon with each voxel $j = 1$ to N : $(L, T)_{ij}$, where L_{ij} is the muon path length inside each voxel and T_{ij} is the 3D path length from the exit point of the voxel to the exit point of the probed volume, as seen in Section B.2;

3. For each muon voxel pair, compute the weight matrix: W_{ij} defined in Equation B.12, which takes into account the geometry of interaction;

4. Initialise the λ in each voxel with a guess: λ_{AIR};

5. Do until (stopping criteria):

   (a) for each muon, compute $\Sigma_{D_i}^{-1}$, which is the inverse of the covariance matrix defined in Equation B.11;

   (b) for each muon voxel pair, compute S_{ij}^{n}, which is a conditional expectation term found using Equation B.22;

   (c) find $\lambda_{j,new}$ for each voxel with an iterative method explained in Equation B.24;

6. End do.

The algorithm has been run for 100 iterations and it is approximately 4 times slower than the INFN one, but the quality of the results is encouraging. Figure 4.2(a) shows the slice at z = 0.54 m of a 10 cm uranium target inside a container: the target can be easily distinguished from the background.
However, looking at the curves of the FoM in Figure 4.2(b), we can notice that the error bars are larger than the ones found without using the information on the displacement. This is probably due to the size of the voxels and of the target: the target is a 10 cm radius sphere, and the voxels are cubes of dimensions: 13 cm $\times$ 13 cm $\times$ 13 cm. The region of

the target is small compared to the voxel size, and this creates problems in evaluating the quality of this new algorithm. Thus, we decided to move to a 30 cm target in order to proceed with the analysis.
Figure 4.2(c) shows the slice at z = 0.54 m of a 30 cm uranium target inside a container: the presence of the target is even clearer than before. Comparing this plot to Figure 4.2(d), reconstructed with the Maximum Likelihood Scattering algorithm (MLS), it is evident that the Maximum Likelihood Scattering and Displacement (MLSD) represents an improvement. However, Figure 4.2(e) which is evaluated using the true energy information is still the best image of the probed volume we have.

4.3 MLSD and energy evaluation

Chapter 3 explains in depth the research for the most effective muon momentum estimation. After trying different techniques, we found that using a simple "veto" underneath the detector will produce a significant improvement in the quality of our results. Now, we can try to add this information to the scattering and displacement algorithm.
The research for the best threshold has been performed in the same way as described in Subsection 3.4.2, looking at:

- $E_0 = 5$ GeV : $< E >_{BELOW} = 1.6$ GeV, $< E >_{ABOVE} = 8.5$ GeV;
- $E_0 = 4$ GeV : $< E >_{BELOW} = 1.4$ GeV, $< E >_{ABOVE} = 6.9$ GeV;
- $E_0 = 3$ GeV : $< E >_{BELOW} = 1.3$ GeV, $< E >_{ABOVE} = 5.4$ GeV;
- $E_0 = 2$ GeV : $< E >_{BELOW} = 1$ GeV, $< E >_{ABOVE} = 4$ GeV;
- $E_0 = 1.5$ GeV : $< E >_{BELOW} = 0.8$ GeV, $< E >_{ABOVE} = 3.4$ GeV;
- $E_0 = 1.25$ GeV : $< E >_{BELOW} = 0.7$ GeV, $< E >_{ABOVE} = 3$ GeV;

Figure 4.3(c) shows the curves of the FoM in the cases specified above. Even though the curves are close to each other, the best threshold in the case of the MLSD algorithm is at 2 GeV.
As an example, Figure 4.3(a) represents the slice at z = 0.54 m of a 30 cm uranium sphere inside a steel container, reconstructed using the MLSD algorithm and the energy threshold at $E_0 = 1.25$ GeV (see Subsection 3.4.2 for further details). Comparing Figure 4.3(a) to Figure 4.3(b) (obtained with MLS and energy threshold $E_0 = 1.25$ GeV), it is easy to see

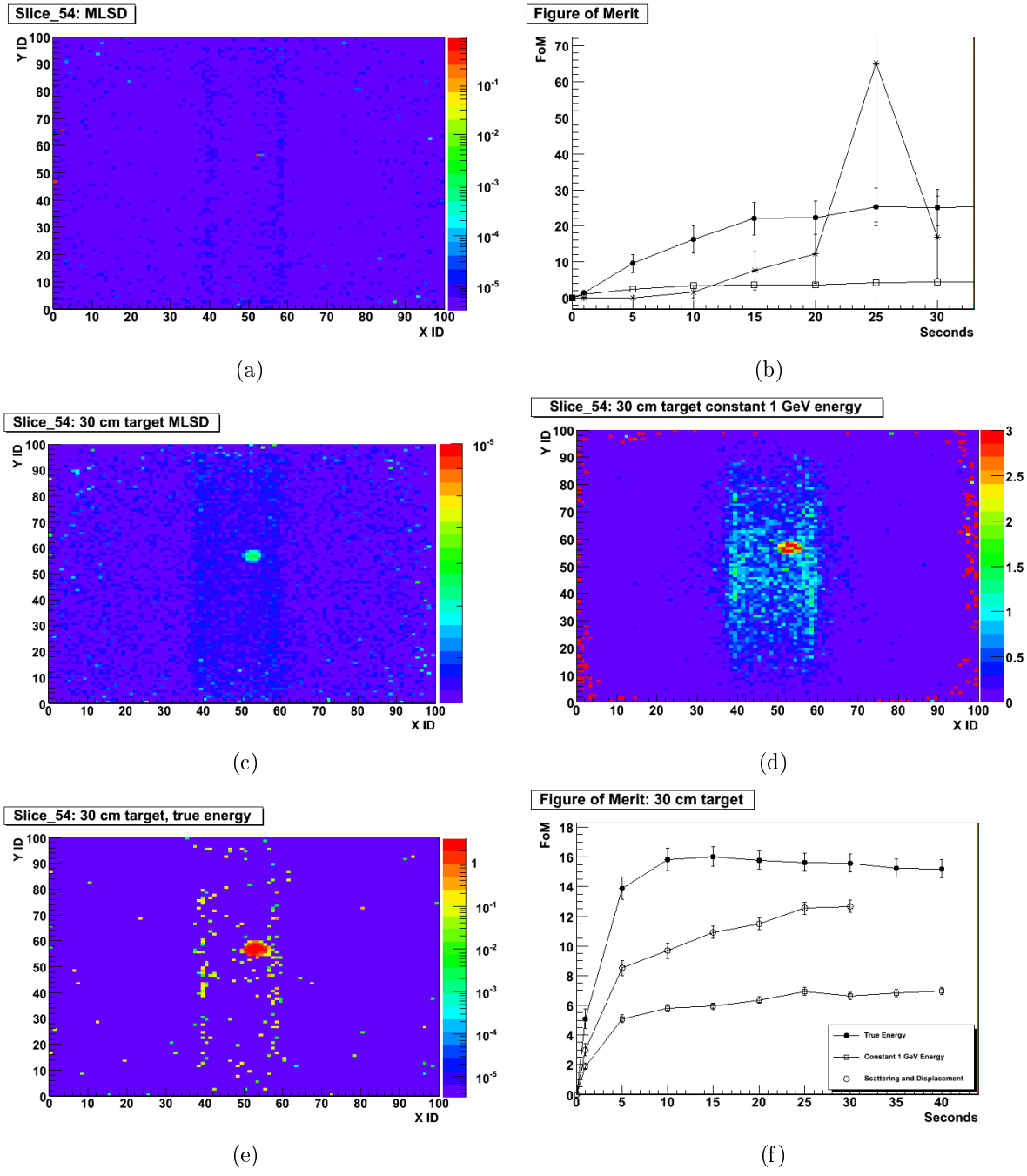

Figure 4.2: (a) Slice at z = 0.54 m of 10 cm uranium sphere in steel container with 15 seconds muon exposure, image reconstructed with MLSD; (b) Curves of the FoM: • true Energy with 10 GeV threshold, □ constant 1 GeV energy, ∗ MLSD; (c), (d) and (e) Slices at z = 0.54 m of 30 cm uranium sphere in steel container with 15 seconds muon exposure, image reconstructed constant 1 GeV energy with MLSD (c), constant 1 GeV energy with MLS (d) and true energy with MLS (e); (f) Curves of the FoM: • true Energy with 10 GeV threshold with MLS, □ constant 1 GeV energy with MLS, ∗ constant 1 GeV energy with MLSD.

the improvement.
Finally, Figure 4.4 highlights this improvement even further: $\square$ represents where we were at the beginning (MLS with constant 1 GeV energy), $\bullet$ represents where we wanted to arrive and $\circ$, $\triangle$ and $*$ represent the steps of the techniques explained through this report. Combining the MLSD technique with the evaluation of the energy with a simple threshold (in this case 2 GeV) can lead to significant improvement in the reconstruction algorithm, so that we can obtain a high quality image of the probed volume with a relatively small exposure time (between 5 and 15 seconds).
Nonetheless, we should not forget that these methods were tested just for 10 cm and 30 cm target; the next step should be trying to optimise the reconstruction algorithm for smaller targets (5 cm or 7 cm) even shielded by disturbing objects (a steel box or a water tank). But before doing that, it is necessary to find a new way to divide the probed volume into voxels in order avoid having the size problem found at the beginning of this Chapter. A possible way to do this could be to divide the probed volume in bigger size voxels and evaluate an average λ value, select one or just few voxels with the maximum λ and divide that volume into smaller voxels.
However, Figure 4.4 emphasises clearly the improvement achieved using the scattering and displacement together with the energy threshold: even though the algorithm is four time slower than the INFN one, the FoM is four times larger.

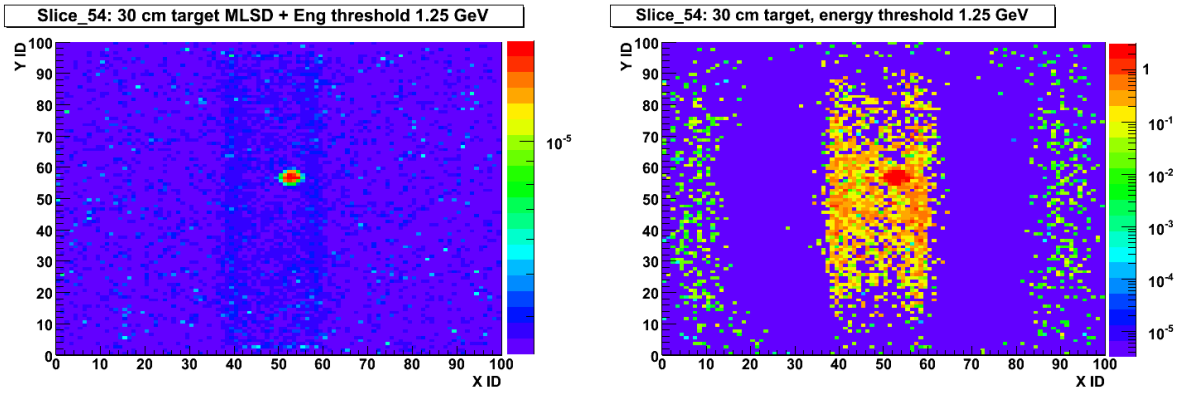

(a) (b)

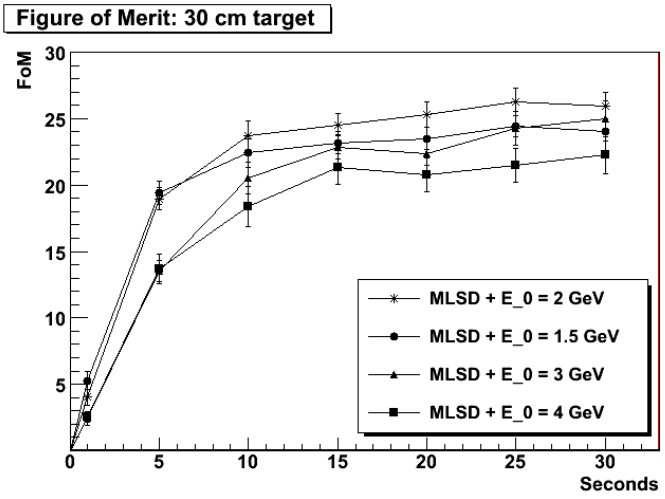

(c)

Figure 4.3: (a) and (b) Slices at z = 0.54 m of 30 cm uranium sphere positioned at (0.5, 1, 0.5) in steel container (2.44 m × 12.15 m × 2.59 m) with 15 seconds muon exposure, image reconstructed with MLSD + energy threshold at $E_0 = 1.25$ GeV (a) and MLS + energy threshold at $E_0 = 1.25$ GeV (b); (c) Curves of the FoM: • MLS true Energy with 10 GeV threshold, □ MLS constant 1 GeV energy, ∘ MLS + $E_0 = 1.25$ GeV, △ MLSD constant 1 GeV energy, ∗ MLSD + $E_0 = 1.25$ GeV.

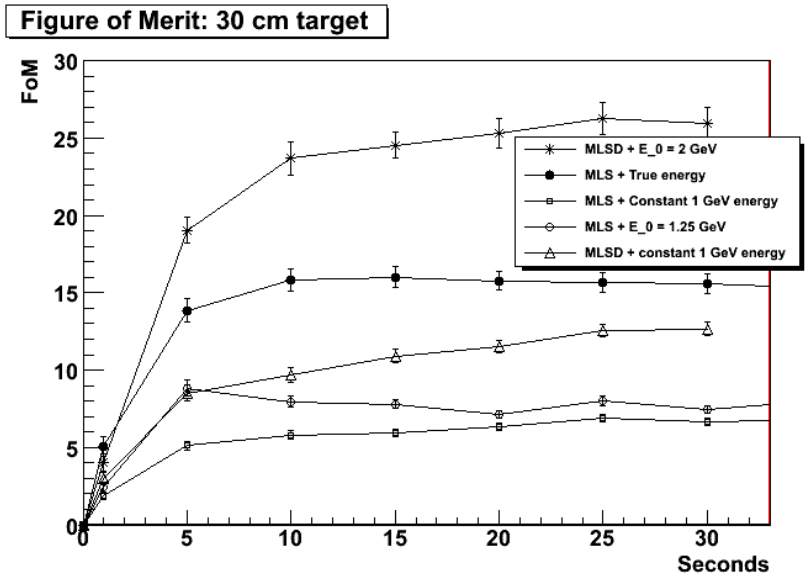

Figure 4.4: Curves of the FoM: • MLS true Energy with 10 GeV threshold, □ MLS constant 1 GeV energy, ∘ MLS + $E_0 = 1.25$ GeV, △ MLSD constant 1 GeV energy, ∗ MLSD + $E_0 = 1.25$ GeV.

Conclusions

In this report we have seen that cosmic ray muons come almost isotropically to the Earth's surface. They are a completely natural and harmless radiation and they can travel very long distances before decaying, hence they are suitable for use in performing tomography and probe images that could not be seen otherwise.
The principle of muon tomography is simple: looking at the Multiple Coulomb Scattering of a muon through a non-homogeneous material, it is possible to have a tomographic image of it .
Different experiments all around the world have proved the importance and the efficiency of this technique and the CREAM TEA experiment aims to improve it for anti-terrorism applications.
In Chapter 3, we saw the importance of evaluating the muon energy, the improvement that can be obtained, the precision needed in the measurements and how this can be achieved by means of different methods. Unfortunately, the time of flight (Subsection 3.4.1) cannot be evaluated with the time precision available with CREAM TEA and the reconstruction obtained with the energy deposited by muons in each strip (Subsection 3.4.3) give just an average of the muon momentum. Nonetheless, it is possible to get a good estimation of the energy using a fit quality parameter (Subsection 3.4.4) which takes into account the scattering inside the scintillator planes.
Sometimes, the best results can be achieved with the simplest method, and this was the case. Using a "veto" underneath the detector we can discern muons into two zones of energy ($E \leq E_0$ or $E \geq E_0$) of which we consider the average energy. By means of this simple but efficient method we can produce high quality results with a lower exposure time with respect to the previous algorithm.
The second step of this Thesis was explained in Chapter 4, where we saw the Maximum Likelihood Scattering and Displacement reconstruction. The algorithm used so far took information just on the scattering angle; this new algorithm takes into account the dis-

placement of the ray together with the scattering angle. Unfortunately, the running time is 4 times slower than the old algorithm, but the quality of the results is improved considerably (we need to remember that one of the aims is to reduce the exposure time, i.e. the number of muons necessary to have a good image of the probed volume; the running time can be reduced with other computational techniques).
The final step was using these two methods together and looking at the best threshold in the case of the MLSD algorithm. The results found are encouraging: the FoM is 4 times larger than using the old algorithm.
The last result has been found using a 30 cm target and one of the next steps is trying to write an efficient algorithm with smaller targets even shielded by water tanks or steel boxes. Although smaller targets can create problems with the voxel size (13 cm $\times$ 13 cm $\times$ 13 cm), it will be possible to overcome this problem by dividing the probed volume in small number of preliminary big voxels, evaluate an average λ value in each of them and select one or a few big voxels to divide into 10^6 smaller voxels. On the other hand, it will be important to speed up the running time of the reconstruction algorithm.

Appendix A

Geometry and code for energy estimation

In this chapter I describe the geometry study and the pieces of code I had to write in order to arrive at an energy estimation.

A.1 Geometry of the strips

Firstly, I need to explain the geometry of the strips and how we can measure the path length of the muon in each strip.
Above and below the probed volume there are 8 scintillator planes; each scintillator plane is divided into strips with the shape of a toblerone; even planes are segmented in x direction, odd planes are segmented in y direction. I will explain the geometry in the plane xz and obviously it is the same as in the yz plane.
In Figures A.1 and A.2 we can see the two different situations for muons passing through the strips.
Let us begin focusing on Figure A.1:

- $P_0 = (x_0, z_0)$ is the centre of the strip;
- $A_1 = (x_0, z_0 - d/2)$ is the edge of the triangle;
- $A_2 = (x_0 + b/2, z_0 + d/2)$ is the right point of the base of the triangle;
- $A_3 = (x_0 - b/2, z_0 + d/2)$ is the left point of the base of the triangle;
- γ : x = z$a + b$ is the reconstructed muon path around the strip.

Secondly, we need to find the angular coefficients and equations for α and β:

$$m_\alpha = \frac{z_0 + d/2 - z_0 + d/2}{x_0 + b/2 - x_0} = \frac{2d}{b} \quad m_\beta = \frac{z_0 + d/2 - z_0 + d/2}{x_0 - b/2 - x_0} = -\frac{2d}{b} \tag{A.1}$$

$$\alpha : \mathrm{z} - z_0 + d/2 = \frac{2d}{b}(\mathrm{x}a + b - x_0) \quad \beta : \mathrm{z} - z_0 + d/2 = -\frac{2d}{b}(\mathrm{x}a + b - x_0) \tag{A.2}$$

Hence, the three points we want to find are:

$$\begin{aligned} x_1 &= z_1\, a + b \\ z_1 &= \frac{z_0 - d/2 - \frac{2d}{b}(b - x_0)}{1 + \frac{2d}{b}a} \end{aligned} \qquad \begin{aligned} x_2 &= z_2\, a + b \\ z_2 &= z_0 + d/2 \end{aligned} \qquad \begin{aligned} x_3 &= z_3\, a + b \\ z_3 &= \frac{z_0 - d/2 + \frac{2d}{b}(b - x_0)}{1 - \frac{2d}{b}a} \end{aligned} \tag{A.3}$$

After finding these three points a function checks which of these are in the area of the strip, pick the two points and evaluate the distance between them.
If the strip is upside down just like in Figure A.2, the principal points are:

- $P_0 = (x_0, z_0)$ is the centre of the strip;
- $A_1 = (x_0, z_0 + d/2)$ is the edge of the triangle;
- $A_2 = (x_0 + b/2, z_0 - d/2)$ is the right point of the base of the triangle;
- $A_3 = (x_0 - b/2, z_0 - d/2)$ is the left point of the base of the triangle;
- $\gamma : \mathrm{x} = \mathrm{z}a + b$ is the reconstructed muon path around the strip.

The formulae are very similar to the ones above:

$$m_\alpha = \frac{z_0 + d/2 - z_0 + d/2}{x_0 + b/2 - x_0} = \frac{2d}{b} \quad m_\beta = \frac{z_0 + d/2 - z_0 + d/2}{x_0 - b/2 - x_0} = -\frac{2d}{b} \tag{A.4}$$

$$\alpha : \mathrm{z} - z_0 - d/2 = \frac{2d}{b}(\mathrm{x}a + b - x_0) \quad \beta : \mathrm{z} - z_0 - d/2 = -\frac{2d}{b}(\mathrm{x}a + b - x_0) \tag{A.5}$$

Hence, the three points are:

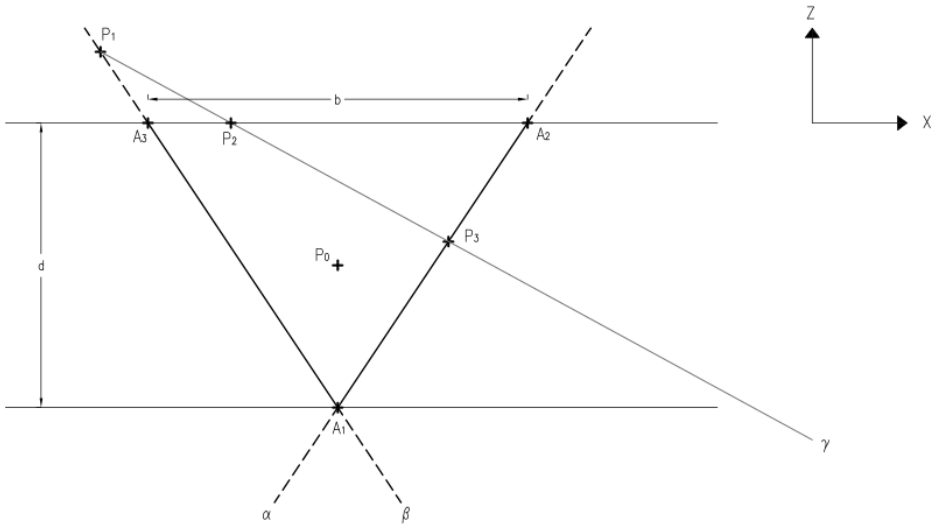

Figure A.1: Geometry of MINERvA strips 1: $P_0 = (x_0, z_0)$ is the centre of the strip; $A_1 = (x_0, z_0 - d/2)$; $A_2 = (x_0 + b/2, z_0 + d/2)$; $A_3 = (x_0 - b/2, z_0 + d/2)$; γ : x = z$a + b$ reconstructed muon path through the strip.

$$
\begin{aligned}
x_1 &= z_1\, a + b \\
z_1 &= \frac{z_0 + d/2 + \dfrac{2d}{b}\,(b - x_0)}{1 - \dfrac{2d}{b}a}
\end{aligned}
\qquad
\begin{aligned}
x_2 &= z_2\, a + b \\
z_2 &= z_0 - d/2
\end{aligned}
\qquad
\begin{aligned}
x_3 &= z_3\, a + b \\
z_3 &= \frac{z_0 + d/2 - \dfrac{2d}{b}\,(b - x_0)}{1 + \dfrac{2d}{b}a}
\end{aligned}
\tag{A.6}
$$

It is evident that just a positive/negative sign before $d/2$ changes from the formulae above to the ones below (notice that z_1 for one kind of strip corresponds to z_3 for the other kind and vice versa).

A.2 Evaluating delta function

The geometry described above can be easily implemented in this function:

```
Double_t Evaluate_delta (double x_0, double z_0, double m, double q, ...
... double m2, double sign){
```

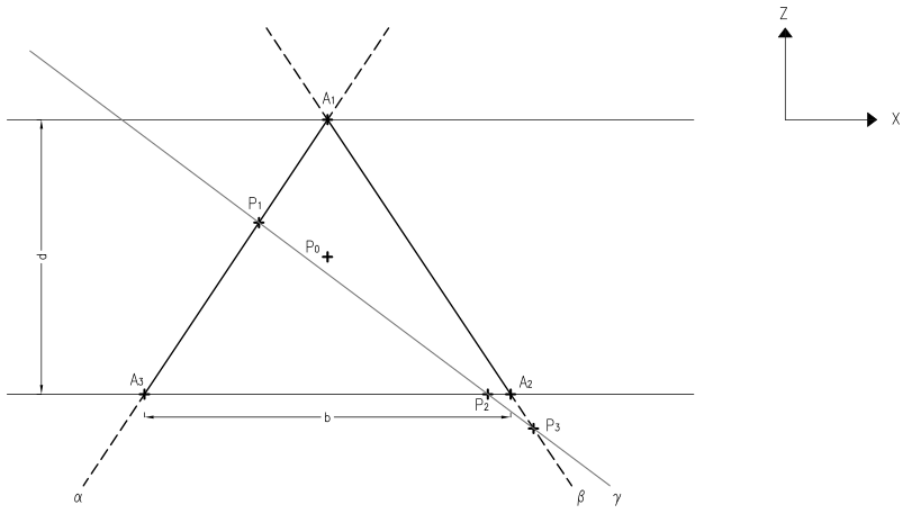

Figure A.2: Geometry of MINERvA strips 2: $P_0 = (x_0, z_0)$ is the centre of the strip; $A_1 = (x_0, z_0 + d/2)$; $A_2 = (x_0 + b/2, z_0 - d/2)$; $A_3 = (x_0 - b/2, z_0 - d/2)$; γ : x = za + b reconstructed muon path through the strip.

```
    Double_t z[3], x[3];
    Double_t delta;
    double d = scintTriHeight*1000.; // in mm
    double b = scintTriBase*1000.; // in mm

    z[0] = (z_0 - (sign*d/2.) + (2*d*(q - x_0)/b) ) / ...
... (1. - (2*d*m/b));
    x[0] = m*z[0] + q;
    z[1] = (z_0 - (sign*d/2.) - (2*d*(q - x_0)/b) )/ ...
... (1. + (2*d*m/b));
    x[1] = m*z[1] + q;
    z[2] = z_0 + (sign*d/2.);
    x[2] = m*z[2] + q;
    int j1 = 0;
    for (int j = 0; j < 3; j++){
     if (x[j] >= (x_0 - (b/2. + 0.1)) && x[j] <= (x_0 + (b/2.+ 0.1))){
      if (z[j] >= (z_0 - (d/2.+ 0.1)) && z[j] <= (z_0 + (d/2.+ 0.1))){
```

```
       x[j1] = x[j];
       z[j1] = z[j];
       j1++;
       }
      }
     }

    if (j1<2) return 0.;
    delta = (sqrt(pow(x[0] - x[1],2.) + ...
... + pow(z[0] - z[1],2.)))*sqrt(1.+m2*m2));
    return delta;
}
```

With regards to the mean and RMS I have used the statistical definition:

$$< x >= \frac{1}{N}\sum_{i=1}^{N} x_i \quad \sigma = \sqrt{\frac{1}{N}\sum_{i=1}^{N}(x_i - < x >)} \tag{A.7}$$

then implemented this function:

```
 void meanAndRMS (int nPoints, double x[], double meanRMS [2]){

 meanRMS[0] = 0.; // mean
 meanRMS[1] = 0.; // RMS
 for (int h = 0; h < nPoints; h++){
  meanRMS[0] += x];
  meanRMS[1] += (x[h]*x[h]);
  }

 meanRMS[0]/= nPoints;
 meanRMS[1] = sqrt((meanRMS[1]/nPoints) - (meanRMS[0]*meanRMS[0]));

}
```

A.3 Image Quality

In Subsection 2.4.5 we saw the reason why we choose the definition of the Figure of Merit as:

$$\mathrm{FoM} = \frac{\mathrm{S} - \mathrm{B}}{\sigma_{\mathrm{B}}} \tag{A.8}$$

The error on the FoM can be evaluated with a simple derivative and is:

$$\sigma_{\mathrm{FoM}} = \sqrt{\left(\frac{\epsilon_{\mathrm{S}}}{\sigma_{\mathrm{B}}}\right)^2 + \left(\frac{\epsilon_{\mathrm{B}}}{\sigma_{\mathrm{B}}}\right)^2 + \left(\mathrm{FoM}\frac{\epsilon_{\sigma_{\mathrm{B}}}}{\sigma_{\mathrm{B}}}\right)^2} \tag{A.9}$$

where ϵ_{S} is the error on the Signal mean, ϵ_{B} is the error on the Background mean and $\epsilon_{\sigma_{\mathrm{B}}}$ is the error on the Background RMS.
This is the code written to evaluate it:

```
#include "DetectorDefs.hh"
#include <cmath>
#include <iostream>

using namespace std;

void  imageQuality () {

  TObjArray *HlistSignal = new TObjArray(20);
  TObjArray *HlistBackground = new TObjArray(20);

  TGraphErrors *FoM_graph = new TGraphErrors();

  char HistName[80];
  char FileName[180];
  char HistoSign[80];
  char HistoBack[80];

  int noBinsX = 100;
  int noBinsY = 100;
  int noBinsZ = 100;
  double side_length = SIDELENGTH;
```

```
double dx = side_length/noBinsX;
double dy = side_length/noBinsY;
double dz = side_length/noBinsZ;

double sphere_radius = SPHERE_RADIUS_CM/100.; // everything in m
double sphere_x = SPHERE_X_M ;
double sphere_y = SPHERE_Y_M ;
double sphere_z = SPHERE_Z_M ;

// half of container dimensions in m
double container_x = (2.44/2);
double container_y = (12.15/2);
double container_z = (2.59/2);

// Number of bins inside the container
int in_x = (noBinsX/2) - int(container_x/dx)  ;
int fin_x = (noBinsX/2) + int(container_x/dx)  ;
int in_y = (noBinsY/2) - int(container_y/dy)  ;
int fin_y = (noBinsY/2) + int(container_y/dy)  ;
int in_z = (noBinsZ/2) - int(container_z/dz)  ;
int fin_z = (noBinsZ/2) + int(container_z/dz)  ;

//Normalise the position of the sphere to the slice coordinates
sphere_x = (sphere_x + (side_length/2.));
sphere_y = (sphere_y + (side_length/2.));
sphere_z = (sphere_z + (side_length/2.));
sphere_radius += sqrt((dx*dx)+(dy*dy)+(dz*dz))/2.;

double x_pos = dx/2.;
double y_pos = dy/2.;
double z_pos = dz/2.;
double distance = 0.;
int point = 1 ;
```

```
  char *input="/Directory/Lambda_10iterations_5cmtarget";

  for (int NFile = 1; NFile < 41 ; NFile ++) {
  if (NFile == 1 || NFile%5 == 0 ) {
  sprintf(FileName,"%s_%d_seconds.root",input,NFile);
  TFile* in = new TFile(FileName);
  sprintf(HistoSign, "%s_%d", "Signal", NFile);
  sprintf(HistoBack, "%s_%d", "Background", NFile);

  //Histo for Current Signal and Current Background
  TH1F *CS = new TH1F(HistoSign, HistoSign,100,0.,10.);
  TH1F *CB = new TH1F(HistoBack, HistoBack,100,0.,10.);

  HlistSignal->Add(CS);
  HlistBackground->Add(CB);

   for(int SliceNo = in_z; SliceNo <= fin_z; SliceNo++){
    sprintf(HistName,"Slice_%d",SliceNo);
    TH2D* CurrentSlice = (TH2D*) in->Get(HistName);
    z_pos = dz*(SliceNo*1. + 0.5);

    for(int x = in_x; x <= fin_x; x++){
   x_pos = dx*(x*1. + 0.5);
      for(int y = in_y; y <= fin_y; y++){
   y_pos = dy*(y*1. + 0.5);
   distance = sqrt(pow((x_pos - sphere_x),2.) + ..
.. + pow((y_pos - sphere_y),2.) + pow((z_pos - sphere_z),2.) ) ;
         if (distance < = sphere_radius){
    CS->Fill(CurrentSlice->GetBinContent(x,y));
   } else CB->Fill(CurrentSlice->GetBinContent(x,y));
      } // end for y
    } // end for x
  } // end slices z
```

```
  double FoM = (CS->GetMean() - CB->GetMean())/ CB->GetRMS();
  double termSign = pow(CS->GetMeanError()/CB->GetRMS(), 2.);
  double termBack = pow(CB->GetMeanError()/CB->GetRMS(), 2.);
  double termSigmaBack = pow(CB->GetRMSError()*FoM/CB->GetRMS(), 2.);
  double FoMerror = sqrt(termSign + termBack + termSigmaBack);

  FoM_graph->SetPoint(point, NFile*1., FoM);
  FoM_graph->SetPointError(point, 0., FoMerror);
  point ++;

  } }

  TFile* out = new TFile("File.root", "RECREATE");

  HlistSignal->Write();
  HlistBackground->Write();
  FoM_graph->SetTitle("Figure of Merit");
  FoM_graph->SetName("FoM_graph");
  FoM_graph->GetXaxis()->SetTitle("Seconds");
  FoM_graph->GetYaxis()->SetTitle("FoM");
  FoM_graph->Write();

  out->Close();

}
```

Appendix B

Geometry and code for scattering and displacement technique

In this Appendix I describe the geometry and the code for the Maximum Likelihood Scattering and Displacement, as described in Chapter 4.

B.1 Evaluating the displacement

In order to understand how to calculate the displacement of a scattered ray, we can refer to Figure B.1. The straight line extension of the unscattered muon path through the volume to the point (x_p, y_p) in Figure B.1 can be defined as:

$$L = \frac{x}{\cos\theta_{x0}\cos\theta_{y0}} = x\sqrt{(1+\tan\theta_{x0}^2)(1+\tan\theta_{y0}^2)} \simeq x\sqrt{1+\tan\theta_{x0}^2+\tan\theta_{y0}^2} = xL_{xy} \tag{B.1}$$

The scattering angle on the x plane is defined as:

$$\Delta\theta_x = \theta_{x1} - \theta_{x0} \tag{B.2}$$

The measured displacement is found as $\Delta x_m = x_1 - x_p$, and must be rotated into the plane orthogonal to the ray path and adjusted for the 3-D path length.
First of all we define:

$$a = \Delta x_m \cos\theta_{x0} \qquad b = \Delta x_m \sin\theta_{x0} \tag{B.3}$$

Hence, Δx in Figure B.1 can be calculated as:

$$\Delta x = b \tan \Delta\theta_x - a = \Delta x_m \left(\frac{\sin \Delta\theta_x}{\cos \Delta\theta_x} \sin \theta_{x0} - \cos \theta_{x0} \right) = \Delta x_m \frac{\cos(\Delta\theta_x + \theta_{x0})}{\cos \Delta\theta_x} \tag{B.4}$$

Now that our measurement is projected with the right orientation, we can adjust it for the 3-D path length by multiplying by $\cos \theta_{y0}$, hence:

$$\Delta x = \Delta x_m \frac{\cos(\Delta\theta_x + \theta_{x0})}{\cos \Delta\theta_x} \cos \theta_{x0} L_{xy} \tag{B.5}$$

In this way, we can redefine the covariance matrix A of Eq. 4.7 as:

$$A = \begin{bmatrix} L & L^2/2 \\ L^2/2 & L^3/3 \end{bmatrix} \tag{B.6}$$

Since scattering measurements are made independently in the two orthogonal planes, we can use the same procedure for the y plane.
It is important to underline that the approximations made in the derivation above are valid only for "small" scattering angles and displacements.

B.2 Scattering through multiple layers of material

Figure B.2 shows a muon trajectory through a non-homogeneous material. The observed information are $\Delta\theta$ and Δx. Actually the muon is undergoing Multiple Coulomb scattering and the "hidden" scattering and displacement in each voxels are $\Delta\theta_j$ and Δx_j.
These quantities are related as:

$$\begin{aligned} \Delta\theta &= \Delta\theta_1 + \Delta\theta_2 + \Delta\theta_3 \\ \Delta x &= \Delta x_1 + L_2 \tan(\Delta\theta_1) + \Delta x_2 + L_3 \tan(\Delta\theta_1 + \Delta\theta_2) + \Delta x_3 \\ &\approx \Delta x_1 + \Delta x_2 + \Delta x_3 + T_1 \Delta\theta_1 + T_2 \Delta\theta_2 \end{aligned} \tag{B.7}$$

Where the latter simplification is valid only for small deflections, and T_j is defined as the 3D ray path length from the exit point of the voxel to the exit point of the probed volume.

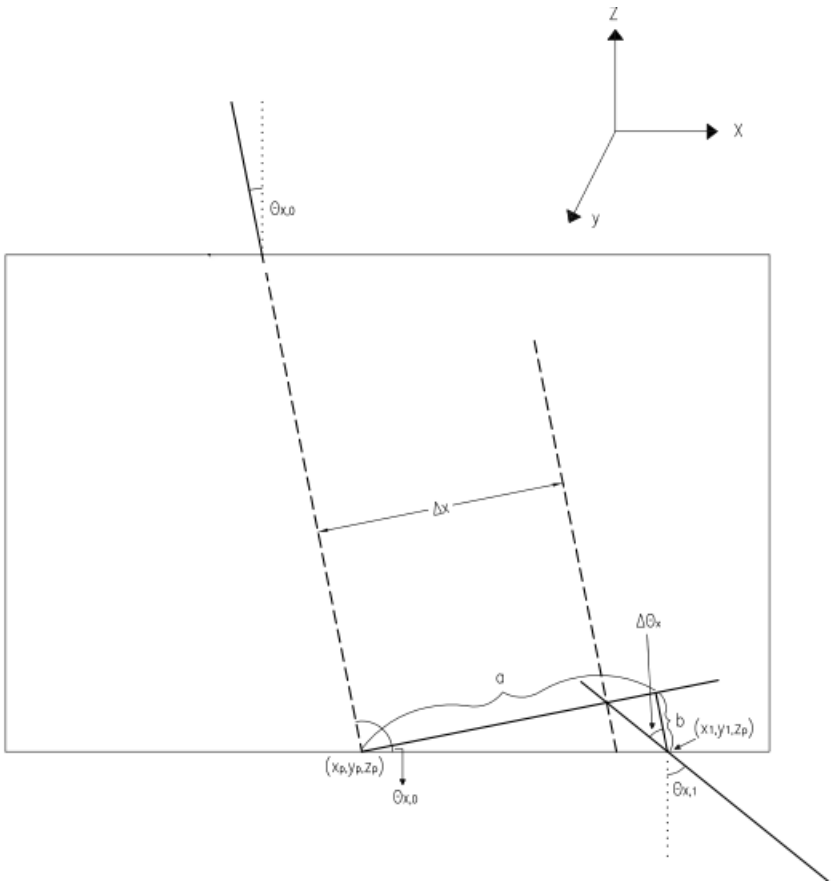

Figure B.1: Projection of the muon path inside the probed volume and definition of scattering displacement.

More generally, we can define:

$$\begin{aligned} \Delta\theta &= \sum_j \Delta\theta_j \\ \Delta x &= \sum_j (\Delta x_j + T_j \Delta\theta_j) \end{aligned} \tag{B.8}$$

Now, we can write the covariance of the scattering and displacement for the i-th ray in the j-th voxel as:

$$\Sigma_{ij} = p_{r,i}^2 \lambda_j A_{ij} \tag{B.9}$$

where $p_{r,i} = \dfrac{13.6}{p_i}$ and:

$$A_{ij} \equiv \begin{bmatrix} L_{ij} & L_{ij}^2/2 \\ L_{ij}^2/2 & L_{ij}^3/3 \end{bmatrix} \tag{B.10}$$

and L_{ij} is the i-th muon path length through the j-th voxel.
Now, we can combine all the equation above and find:

$$\Sigma_i = p_{r,i}^2 \sum_{j \leq N} \lambda_j W_{ij} \tag{B.11}$$

where N is the number of voxels and W_{ij} is a weight matrix defined as

$$W_{ij} \equiv \begin{bmatrix} L_{ij} & L_{ij}^2/2 + L_{ij}T_{ij} \\ L_{ij}^2/2 + L_{ij}T_{ij} & L_{ij}^3/3 + L_{ij}^2 T_{ij} + L_{ij}T_{ij}^2 \end{bmatrix} \tag{B.12}$$

based on a calculation derived in Ref. [22].
Finally, we can define the data vector:

$$D_i \equiv \begin{bmatrix} \Delta\theta_i \\ \Delta x_i \end{bmatrix} \tag{B.13}$$

Hence, the likelihood of λ can be written as:

$$P(D|\lambda) = \prod_{i \leq M} P(D_i|\lambda) \tag{B.14}$$

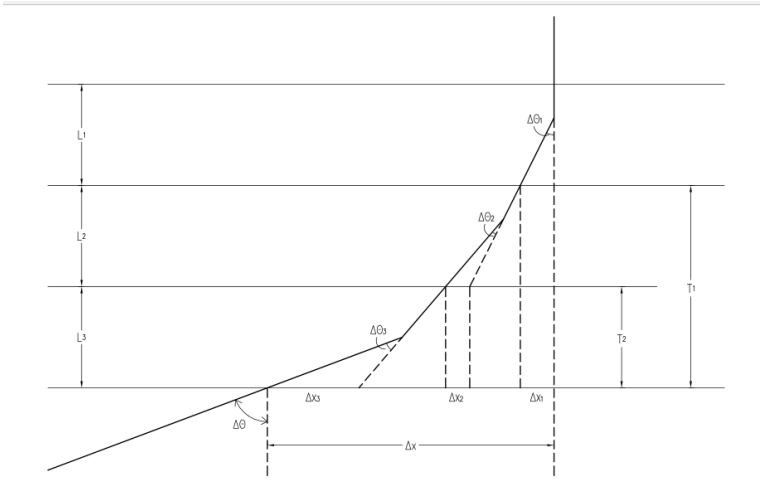

Figure B.2: Muon scattering through different materials (magnitude of scattering is exaggerated).

where i is the muon number that goes from 1 to M, and the factors are:

$$P(D_i|\lambda) = \frac{1}{2\pi|\Sigma_i|^{1/2}} \exp\left(-\frac{1}{2} D_i^T \Sigma_i^{-1} D_i\right) \tag{B.15}$$

B.3 Maximum Likelihood Expectation Maximisation

The Maximum Likelihood technique from an incomplete set of data through the Expectation Maximisation is explained in Ref. [21]. This algorithm relies on two data sets: "incomplete" (i.e. observed) and "complete" (i.e. hidden plus observed) data.
In this context, the first set of data is the measured scattering and displacement: $D = \{D_i : 1 \leq i \leq M\}$. The latter is represented by the set of scattering angle and displacement of the i-th muon by the j-th voxel: $H = \{H_{ij} : 1 \leq i \leq M \& 1 \leq j \leq N\}$.
The algorithm uses an auxiliary function:

$$Q = \mathbb{E}_{H|D,\lambda^n}[\log(P(D, H|\lambda))] = \mathbb{E}_{H|D,\lambda^n}[\log(P(H|\lambda))] \tag{B.16}$$

where the second passage is because the hidden data determine the observed data uniquely. This auxiliary function is the expected value of the log likelihood of the observed and hidden data, given the parameter vector λ and λ^n with respect to the conditional distribution of

H [13].
Two steps were performed for each iteration:

1. Estimate the conditional distribution of hidden data $P(D, H|\lambda)$;
2. Maximise the auxiliary function Q, which is an expected value with respect to the distribution found in step 1.

From the parameter λ^n, the algorithm produces a new estimation λ^{n+1}:

$$\lambda^{n+1} = \arg\max_{\lambda} Q(\lambda; \lambda^n) \tag{B.17}$$

Now we can start writing the probability distribution, similar to Equation B.15:

$$P(H_{ij}|\lambda) = \frac{1}{2\pi|\Sigma_{ij}|^{1/2}} \exp\left(-\frac{1}{2} H_{ij}^T \Sigma_{ij}^{-1} H_{ij}\right) \tag{B.18}$$

where Σ_{ij} is defined in Equation B.9.
Since the distribution of scattering in each voxel is independent of the scattering in other voxels, the overall probability of the set of hidden data is the product of each probability in Equation B.18. Hence, the log likelihood can be written as:

$$\log(P(H|\lambda)) = \sum_{j \leq N} \sum_{i:L_{ij} \neq 0} \left(-\log \lambda_j - \frac{H_{ij}^T A_{ij}^{-1} H_{ij}}{2\lambda_j p_{r,i}^2}\right) + C \tag{B.19}$$

where $p_{r,i} = 13.6/p_i$ is the factor seen in Equation 4.1 and $C = -\log(2\pi) - 2\log p_{r,i} - \log|A_{ij}|$ is a sum of constant terms not containing λ.
The procedure for arriving at the conditional expectation is explained in Ref. [13], where we find that the Q function is:

$$Q(\lambda; \lambda^n) = C + \sum_{j \leq N} \left(-M_j \log \lambda_j - \frac{1}{2\lambda_j} \sum_{i:L_{ij} \neq 0} S_{ij}^n\right) \tag{B.20}$$

where M_j is the number of muons for which $L_{ij} \neq 0$ and S_{ij}^n is defined as:

$$S_{ij}^n \equiv \mathbb{E}_{H|D,\lambda^n}[p_{r,i}^{-2} H_{ij}^T A_{ij}^{-1} H_{ij}] \tag{B.21}$$

Ref. [13] explains through a lengthy but easy calculation how to get S_{ij}^n as:

$$S_{ij}^n = 2\lambda_j^n + (D_i^T \Sigma_{D_i}^{-1} W_{ij} \Sigma_{D_i}^{-1} D_i - \mathrm{Tr}(\Sigma_{D_i}^{-1} W_{ij})) \times p_{r,i}^2 \left(\lambda_j^n\right)^2 \tag{B.22}$$

where D_i is the data vector defined at the beginning of this section, Σ_{D_i} is the matrix defined in Equation B.11 and W_{ij} is defined in Equation B.12.
Before using this expression of S_{ij}^n, it is necessary to incorporate the x and y information with a simple average as:

$$S_{ij}^n = \frac{S_{ij,x}^n + S_{ij,y}^n}{2} \tag{B.23}$$

Finally, differentiating Equation B.20 with respect to λ_j, considering S_{ij}^n almost constant, we find the iterative formula to update the value of λ as:

$$\lambda_j^{n+1} = \frac{1}{2M_j} \sum_{i:L_{ij}\neq 0} S_{ij}^n \tag{B.24}$$

B.4 From MLS to MLSD algorithm

The first step done was the evaluation of $\Delta\theta_x$, $\Delta\theta_y$, Δx and Δy, done in the PCA algorithm which can be found in the file `makePCAfile.cxx` in Ref. [23]. The new version `makePCAfileMLSD.cxx` has a similar piece of code repeated 4 times (for x and y plane, for the true and reconstructed variables):

```
float a1 = xzGradTrue[0];
float a2 = xzGradTrue[1];
float modp = sqrt(1.0+a1*a1);  // 1/cos(theta0)
float modq = sqrt(1.0+a2*a2);  // 1/cos(theta1)
thetaxzTrue = atan((a1 - a2)/(1.0 + a1*a2));
double Lxy = sqrt(1. + (a1*a1) + (yzGradTrue[0]*yzGradTrue[0]));
double xp = xzGradTrue[0]*(-verticalSeparation*1000./2.) + xzCutTrue[0];
double x1 = xzGradTrue[1]*(-verticalSeparation*1000./2.) + xzCutTrue[1];
dxTrue = (xp - x1)*Lxy/(cos(thetaxzTrue)*modp*modq);
```

Before starting the code for the MLSD algorithm it is convenient to set a number of definitions:

$$
\begin{aligned}
P =& D_i^T \Sigma_{D_i}^{-1} W_{ij} \Sigma_{D_i}^{-1} D_i \\
W_{ij} =& \begin{bmatrix} L_{ij} & L_{ij}^2/2 + L_{ij}T_{ij} \\ L_{ij}^2/2 + L_{ij}T_{ij} & L_{ij}^3/3 + L_{ij}^2 T_{ij} + L_{ij}T_{ij}^2 \end{bmatrix} = \begin{bmatrix} L_{ij} & B_{ij} \\ B_{ij} & C_{ij} \end{bmatrix} \\
\Sigma_{D_i}^{-1} =& \begin{bmatrix} aD_i & bD_i \\ bD_i & cD_i \end{bmatrix} \\
aD_i =& \frac{p_{r,i}^2}{|\Sigma_{D_i}|} \sum_{j \leq N} \lambda_j C_{ij} \\
bD_i =& -\frac{p_{r,i}^2}{|\Sigma_{D_i}|} \sum_{j \leq N} \lambda_j B_{ij} \\
cD_i =& \frac{p_{r,i}^2}{|\Sigma_{D_i}|} \sum_{j \leq N} \lambda_j L_{ij} \\
|\Sigma_{D_i}| =& p_{r,i}^2 \left(\left(\sum_{j \leq N} \lambda_j L_{ij} \right) \left(\sum_{j \leq N} \lambda_j C_{ij} \right) + \left(\sum_{j \leq N} \lambda_j B_{ij} \right)^2 \right)
\end{aligned}
\tag{B.25}
$$

The MLS algorithm is described in Subsection 2.4.4 and in Ref. [12]. It relies on three files written by William Brigg last year: `GenerateLambdaMap.cpp`, `LambdaPcaTreeLooper.h` and `LambdaPcaTreeLooper.C`, which can be found in Ref. [23].
`GenerateLambdaMap.cpp` contains a Parabolic Interpolation with Brent's method in 1D from Ref. [24] which minimises the cost function defined in Subsection 2.4.4. Since the MLSD algorithm relies on Equation B.24 and does not need a maximisation (or minimisation of $\psi = -Q(\lambda; \lambda^n)$ as in the INFN algorithm). For this reason, instead of the Brent iteration the new `GenerateLambdaMapMLSD.cpp` file contained:

```
int iterations = 100;
LambdaPcaTreeLooperMLSD targetLooperMLSD(targetTree);
targetLooperMLSD.SLFill(0,muons,Nx,Ny,Nz);
targetLooperMLSD.LambdaFill(Nx*Ny*Nz);
targetLooperMLSD.SigmaFill();

for(int iii = 0; iii < iterations; iii++){
  fx=targetLooperMLSD.Cost(0.1,0,muons);
```

```
    targetLooperMLSD.LambdaNew();
    targetLooperMLSD.SigmaFill();
  }
  targetLooperMLSD.DrawSlices(100,1,Nx,Ny,Nz,fileNameLambda);
```

The second step was updating the header file to `LambdaPcaTreeLooperMLSD.h` adding the definitions of new variables and functions as defined below:

- T map of a map: corresponds to T_{ij}, the 3D ray path length from the exit point of the voxel to the exit point of the probed volume;
- B map of a map: corresponds to $B_{ij} = L_{ij}^2/2 + L_{ij}T_{ij}$;
- C map of a map: corresponds to $C_{ij} = L_{ij}^3/3 + L_{ij}^2 T_{ij} + L_{ij}T_{ij}^2$;
- S vector: corresponds to $S_j = \sum_{i:L_{ij}\neq 0} S_{ij}^n$;
- M vector: corresponds to $M_j = \sum_{i:L_{ij}\neq 0} 1$;
- $\Delta\theta_x$, $\Delta\theta_y$, Δx and Δy vectors: correspond to scattering angles and displacements;
- aD, bD and cD vectors: correspond to the definitions in Equation B.25

The piece of code is simply:

```
std::map <int, std::map<int, double> > T;
std::map <int, std::map<int, double> > B;
std::map <int, std::map<int, double> > C;
double *S; // S_i is not the scattering angle!!!
double *M;
double *dThetax;
double *dThetay;
double *dx;
double *dy;
double *aD;
double *bD;
double *cD;
virtual void LambdaNew();
virtual void mm_mul (double A[][2], double B[][2], double C[][2]);
```

To go from `LambdaPcaTreeLooper.C` to `LambdaPcaTreeLooperMLSD.C` the modifications were many. Firstly, a matrix multiplication function has been added at the beginning of the file, to make it easier to evaluate S_{ij}:

```
void LambdaPcaTreeLooperMLSD::mm_mul (double A[2][2],
 double B[2][2], double C[2][2]){
 int i, j, k;
 double sum;
 for (i = 0; i < 2; i++) {
   for (j = 0; j < 2; j++) {
    sum = 0;
    for (k = 0; k < 2; k++) {
     sum += A[i][k] * B[k][j];
      }
     C[i][j] = sum;
    }
   }
  }
```

Secondly, the function `LambdaPcaTreeLooperMLSD::SLFill` was evaluating L_{ij}, together with T_{ij}, B_{ij} and C_{ij}, and reading the information of scattering angles and displacements: $\Delta\theta_x$, $\Delta\theta_y$, Δx and Δy. This has been done defining a temporary map `tempMapT` with the vertical distance from the centre of the voxel and the bottom of the probed volume, and evaluating for each muon the factor L_{xy} as defined in Equation B.1. At the end of the loop the maps were filled as defined in Equation B.25.
Since the method of uploading the λ value is completely different, I had to write a new function as:

```
void LambdaPcaTreeLooperMLSD::LambdaNew(){
   clock_t LambdaStart = clock();
   double newLambda;
   for(int voxId=0;voxId<fVoxelCount;voxId++) {
      newLambda = S[voxId]/(2.*M[voxId]);
      if(newLambda < LAMBDA_AIR) newLambda = LAMBDA_AIR;
      if(isnan(newLambda)) newLambda = LAMBDA_AIR;
     Lambda[voxId] = newLambda;
```

```
   }
   printf("Lambda Alpha Fill: %f\n",
((double)(clock() - LambdaStart) / CLOCKS_PER_SEC));
}
```

Now, the function that was filling the σ value in the INFN algorithm had to be changed to a function that was filling the vector aD_i, bD_i and cD_i as in Equation B.25. The code is:

```
void LambdaPcaTreeLooperMLSD::SigmaFill(){
 clock_t SigmaStart = clock();
 static int doneInit=0;
 static Double_t determinant=0;
 if(!doneInit) {
    aD = new double[fNumMuons];
    bD = new double[fNumMuons];
    cD = new double[fNumMuons];
    DET = new double[fNumMuons];
 }
 doneInit++;
 memset(aD,0,fNumMuons*sizeof(double));
 memset(bD,0,fNumMuons*sizeof(double));
 memset(cD,0,fNumMuons*sizeof(double));

 for(std::map<int,map<int,double> >::iterator iter1 =
L.begin(); iter1 != L.end(); ++iter1){ //loop over muons
  aD[iter1->first] = 0.;
  bD[iter1->first] = 0.;
  cD[iter1->first] = 0.;
  determinant = 0.;
   //loop over voxels
   for(std::map<int,double>::iterator iter2 = (iter1->second).begin();
 iter2 != (iter1->second).end(); ++iter2){
    cD[iter1->first] += iter2->second * Lambda[iter2->first];
    bD[iter1->first] += B[iter1->first][iter2->first]
*Lambda[iter2->first];
    aD[iter1->first] += C[iter1->first][iter2->first]
```

```
*Lambda[iter2->first];
   }//end loop over voxels
   cD[iter1->first] *= PreFactorEng[iter1->first];
   bD[iter1->first] *= PreFactorEng[iter1->first];
   aD[iter1->first] *= PreFactorEng[iter1->first];
   cD[iter1->first] += 0.000049;
   determinant = (aD[iter1->first]*cD[iter1->first])
 - TMath::Power(bD[iter1->first], 2.);
   aD[iter1->first]/=determinant;
   bD[iter1->first]/=(determinant*(-1.));
   cD[iter1->first]/=determinant;

   } //end loop over muons

   printf("Sigma Fill: %f\n", ((double)(clock() - SigmaStart)
/ CLOCKS_PER_SEC));
}
```

Finally, the function to evaluate the cost function has been modified so as to evaluate S_j and M_j. This can be done with this code:

```
double LambdaPcaTreeLooperMLSD::Cost(double Alpha, int first, int last){

   double cost=0;
   static double mat_W[2][2];
   static double mat_D[2][2]; //SigmaD
   static double mat_R[2][2]; // SigmaD*W
   static double mat_Tot[2][2]; // SigmaD*W*SigmaD
   static double trace;
   static double product;

  static int loopCount=0;
   static double newLambda;
   static int muonNum;
   static double muonCost;
   static double costVoxel;
```

```
   static int madeSM=0;
if(!madeSM){
      S = new double[fVoxelCount];
      M = new double[fVoxelCount];
madeSM++;
}
   memset(S,0,fVoxelCount*sizeof(double));
   memset(M,0,fVoxelCount*sizeof(double));
for(std::map <int, std::map<int, double> >::iterator muonIter=L.begin();
       muonIter!=L.end();
       muonIter++) {
      muonNum=muonIter->first;
 mat_D[0][0] = aD[muonNum];
 mat_D[0][1] = bD[muonNum];
 mat_D[1][0] = bD[muonNum];
 mat_D[1][1] = cD[muonNum];
      for(std::map<int,double>::iterator iter =
(muonIter->second).begin(); iter != (muonIter->second).end(); ++iter){
 newLambda = Lambda[iter->first];
 mat_W[0][0] = iter->second;
 mat_W[0][1] = B[muonNum][iter->first];
 mat_W[1][0] = B[muonNum][iter->first];
 mat_W[1][1] = C[muonNum][iter->first];
  LambdaPcaTreeLooperMLSD::mm_mul (mat_D, mat_W, mat_R);
 trace = mat_R[0][0] + mat_R[1][1];
  LambdaPcaTreeLooperMLSD::mm_mul (mat_R, mat_D, mat_Tot);
 product = (mat_Tot[0][0]*dThetax[muonNum]*dThetax[muonNum]) +
(mat_Tot[1][0]*dThetax[muonNum]*dx[muonNum]) +
(mat_Tot[0][1]*dThetax[muonNum]*dx[muonNum]) +
(mat_Tot[1][1]*dx[muonNum]*dx[muonNum]);
 S[iter->first] += 0.5*(2*newLambda +
(newLambda*newLambda*PreFactorEng[muonNum]*(product-trace)));
//now add the Y component
 product = (mat_Tot[0][0]*dThetay[muonNum]*dThetay[muonNum]) +
```

```
(mat_Tot[1][0]*dThetay[muonNum]*dy[muonNum]) +
(mat_Tot[0][1]*dThetay[muonNum]*dy[muonNum]) +
(mat_Tot[1][1]*dy[muonNum]*dy[muonNum]);
 S[iter->first] += 0.5*(2*newLambda +
(newLambda*newLambda*PreFactorEng[muonNum]*(product-trace)));
 M[iter->first] +=1.;
}
   }
  for(int voxId=0;voxId<fVoxelCount;voxId++) {
costVoxel = M[voxId]*TMath::Log(Lambda[voxId]) +
(S[voxId]*0.5/Lambda[voxId]);
cost+= costVoxel;
}
   loopCount++;
   return cost;
}
```

This function takes as input an α value and gives as output the value of the cost function, even though is not necessary for the implementation of the MLSD algorithm as seen in this report. However, this kind of algorithm could be easily changed with a maximisation evaluating a gradient without changing the form of this function.

Bibliography

[1] Morris *et al.*, "Tomographic imaging with cosmic ray muons," *Science and Global Security*, vol. 16, pp. 37–53, 2008.

[2] L. Schultz, K. Borozdin, J. Gomez, G. Hogan, J. McGill, C. Morris, W. Priedhorsky, A. Saunders, and M. Teasdale, "Image reconstruction and material Z discrimination via cosmic ray muon radiography," *Nuclear Instruments and Methods in Physics Research Section A: Accelerators, Spectrometers, Detectors and Associated Equipment*, vol. 519, no. 3, pp. 687–694, 2004.

[3] E. George, "Commonwealth Engineer," 1955.

[4] L. Alvarez, J. Anderson, F. Bedwei, J. Burkhard, A. Fakhry, A. Girgis, A. Goneid, F. Hassan, D. Iverson, G. Lynch, *et al.*, "Search for hidden chambers in the pyramids," *Science*, vol. 167, no. 3919, p. 832, 1970.

[5] K. Nagamine, M. Iwasaki, K. Shimomura, and K. Ishida, "Method of probing inner-structure of geophysical substance with the horizontal cosmic-ray muons and possible application to volcanic eruption prediction," *Nuclear Instruments and Methods in Physics Research Section A: Accelerators, Spectrometers, Detectors and Associated Equipment*, vol. 356, no. 2-3, pp. 585–595, 1995.

[6] J. Elster and H. Geitel *Phys. Zs.*, no. 2, pp. 116, 560, 1900.

[7] A. Bonetti, I. Guidi, B. Monteleoni, and A. nazionale dei Lincei, *Cosmic ray, particle and astroparticle physics: a conference in honour of Giuseppe Occhialini, Bruno Pontecorvo and Bruno Rossi, Florence, 11-13 september 1995.* Accademia nazionale dei Lincei, 1997.

[8] K. Nakamura *et al.*, "Review of Particle Physics," *Journal of Physics G: Nuclear and Particle Physics*, vol. 37, p. 075021, 2010.

[9] P. Grieder, "Cosmic rays at Earth," 2001.

[10] A. Bettini, *Introduction to elementary particle physics*. Cambridge Univ Pr, 2008.

[11] E. T. Wright, "A detector for muon tomography: Data acquisition and preliminary results," Master's thesis, UT University Texas, May 2007.

[12] S. Pesente, S. Vanini, M. Benettoni, G. Bonomi, P. Calvini, P. Checchia, E. Conti, F. Gonella, G. Nebbia, S. Squarcia, *et al.*, "First results on material identification and imaging with a large-volume muon tomography prototype," *Nuclear Instruments and Methods in Physics Research Section A: Accelerators, Spectrometers, Detectors and Associated Equipment*, vol. 604, no. 3, pp. 738–746, 2009.

[13] L. Schultz, G. Blanpied, K. Borozdin, A. Fraser, N. Hengartner, A. Klimenko, C. Morris, C. Oram, and M. Sossong, "Statistical reconstruction for cosmic ray muon tomography," *Image Processing, IEEE Transactions on*, vol. 16, no. 8, pp. 1985–1993, 2007.

[14] "MINOS at Fermilab." `http://www-numi.fnal.gov/Minos/`.

[15] "MINERvA at Fermilab." `http://minerva.fnal.gov/`.

[16] S. Agostinelli, J. Allison, K. Amako, J. Apostolakis, H. Araujo, P. Arce, M. Asai, D. Axen, S. Banerjee, G. Barrand, *et al.*, "Geant4-a simulation toolkit," *Nuclear Instruments and Methods in Physics Research-Section A Only*, vol. 506, no. 3, pp. 250–303, 2003.

[17] "ROOT Cern." `http://root.cern.ch/drupal/`.

[18] "Particle Data Group." `http://pdg.lbl.gov/`.

[19] "Compact Muon Solenoid, CMS at CERN." `http://cms.web.cern.ch/`.

[20] Y. Liu, Z. Chen, Z. Zhao, L. Zhang, and Z. Wang, "Imaging Algorithms for Cosmic Ray Muon Radiography Detection of Nuclear Materials*," *Tsinghua Science & Technology*, vol. 14, no. 3, pp. 313–321, 2009.

[21] A. Dempster, N. Laird, and D. Rubin, "Maximum likelihood from incomplete data via the em algorithm," *Journal of the Royal Statistical Society. Series B (Methodological)*, vol. 39, no. 1, pp. 1–38, 1977.

[22] L. SCHULTZ, *Cosmic ray muon radiography*. PhD thesis, Portland State University, 2003.

[23] "CREAM TEA code repository." `http://cvs.hep.ucl.ac.uk/trac/creamtea`.

[24] *Numerical recipes in C++: the art of scientific computing*. Numerical recipes, Cambridge University Press, 2002.